The Astrophysical Journal, in press
Preprint typeset using LaTeX style emulateapj v. 04/03/99

arXiv:astro-ph/0012481v2 27 Feb 2001

DIFFUSE GAS AND LMXBS IN THE *CHANDRA* OBSERVATION OF THE S0 GALAXY NGC 1553

Elizabeth L. Blanton[1], Craig L. Sarazin[1], and Jimmy A. Irwin[2,3]

The Astrophysical Journal, in press

ABSTRACT

We have spatially and spectrally resolved the sources of X-ray emission from the X-ray faint S0 galaxy NGC 1553 using an observation from the *Chandra* X-ray Observatory. The majority (70%) of the emission in the $0.3-10.0$ keV band is diffuse, and the remaining 30% is resolved into 49 discrete sources. Most of the discrete sources associated with the galaxy appear to be low mass X-ray binaries (LMXBs). The luminosity function of the LMXB sources is well-fit by a broken power-law with a break luminosity comparable to the Eddington luminosity for a $1.4M_\odot$ neutron star. It is likely that those sources with luminosities above the break are accreting black holes and those below are mostly neutron stars in binary systems. Spectra were extracted for the total emission, diffuse emission, and sum of the resolved sources; the spectral fits for all require a model including both a soft and hard component. The diffuse emission is predominately soft while the emission from the sources is mostly hard. Approximately 24% of the diffuse emission arises from unresolved LMXBs, with the remainder resulting from thermal emission from hot gas. There is a very bright source at the projected position of the nucleus of the galaxy. The spectrum and luminosity derived from this central source are consistent with it being an AGN; the galaxy also is a weak radio source. Finally, the diffuse emission exhibits significant substructure with an intriguing spiral feature passing through the center of the galaxy. The X-ray spectrum and surface brightness of the spiral feature are consistent with adiabatic or shock compression of ambient gas, but not with cooling. This feature may be due to compression of the hot interstellar gas by radio lobes or jets associated with the AGN.

Subject headings: binaries: close — galaxies: elliptical and lenticular — galaxies: ISM — X-rays: galaxies — X-rays: ISM — X-rays: stars

1. INTRODUCTION

There is evidence from their X-ray spectra that a variety of different emission mechanisms contribute to the X-ray luminosity of early-type galaxies. Elliptical and S0 galaxies exhibit varying X-ray spectra that depend on the ratio of the galaxy's X-ray-to-optical luminosity (L_X/L_B), (Kim, Fabbiano, & Trinchieri 1992). X-ray bright E and S0 galaxies (those with high L_X/L_B) emit thermally with a spectrum that is well modeled by an optically thin plasma with a temperature of $kT \approx 1$ keV (Forman, Jones, & Tucker 1985; Canizares, Fabbiano, & Trinchieri 1987). X-ray faint E and S0's (those with low L_X/L_B) have spectra that require a model comprised of two components, soft emission with $kT \approx 0.2$ (Fabbiano, Kim, & Trinchieri 1994) and a hard component (Matsumoto et al. 1997). The hard component has been fit either as thermal bremsstrahlung with $kT \gtrsim 5$ keV (Matsumoto et al. 1997) or a power-law (Allen, di Matteo, & Fabian 2000). The hard component of the spectra for X-ray faint E and S0 galaxies is roughly proportional to the optical luminosity of the galaxy, suggesting that its origin is low-mass X-ray binaries (LMXBs) such as those seen in our Galaxy (Trinchieri & Fabbiano 1985). In some galaxies, a central active galactic nucleus (AGN) may be an important source of hard X-ray emission (Allen et al. 2000). The origin of the soft component remains uncertain (Fabbiano, Kim, & Trinchieri 1994; Pellegrini 1994; Kim et al. 1996; Irwin & Sarazin 1998a,b). It might be due to interstellar gas, LMXBs, some other stellar component, or some other source. Irwin & Sarazin (1998a,b) argued that LMXBs produce much of the soft emission in the most X-ray faint galaxies, while the contribution of interstellar gas increases as L_X/L_B increases. In X-ray faint E and S0 galaxies, much of this hot gas may have been lost in galactic winds or as a result of ram pressure stripping by intragroup or intracluster gas.

Until now, X-ray detectors have not had sufficient spatial resolution to resolve the LMXBs from diffuse emission in most external galaxies. The *Chandra* X-ray Observatory has given us the opportunity to resolve these components spatially and spectrally and to uncover the source of emission from X-ray faint E and S0 galaxies. In this paper, we present a *Chandra* observation of the S0 galaxy NGC 1553. Its L_X/L_B ratio puts it on the bright end of the class of X-ray faint ellipticals and S0's (Irwin & Sarazin 1998b). Although other galaxies have lower L_X/L_B ratios, NGC 1553 was chosen because its high X-ray flux and proximity make it a good candidate for resolving LMXBs with *Chandra*. Another X-ray faint galaxy, NGC 4697, with a lower L_X/L_B ratio was also observed (Sarazin, Irwin, & Bregman 2000). NGC 4697 is closer with a lower X-ray flux and will sample the faint end of the LMXB luminosity function. The L_X/L_B ratio and X-ray colors of NGC 1553 put it in a class of galaxies that Irwin & Sarazin

[1]Department of Astronomy, University of Virginia, P. O. Box 3818, Charlottesville, VA 22903-0818; eblanton@virginia.edu, sarazin@virginia.edu

[2]Department of Astronomy, University of Michigan, Ann Arbor, MI 48109-1090; jirwin@astro.lsa.umich.edu

[3]*Chandra* Fellow

(1998b) hypothesized may have some contribution of hot ISM to the spectrum, that could be fit by a thermal model with $kT = 0.3-0.6$ and metallicity of 10-20% of solar along with a stellar component.

NGC 1553 is interacting with a companion, NGC 1549, as evidenced by shells of emission seen in the optical. The two galaxies are separated by 11.′8 (Bridges & Hanes 1990). NGC 1553 is known to have cool gas and dust associated with it. It was detected in the infrared in all four *IRAS* bands studied in Bally & Thronson (1989). In addition, it is a weak radio source with a flux density of 10 mJy at 843 MHz (Harnett 1987). A dust lane was observed at small scales ($\approx 3''$ across) at the center of the galaxy with HST (Quillen, Bower, & Stritzinger 2000). Previous X-ray observations with the *ROSAT* HRI (Trinchieri, Noris, & di Serego Alighieri, 1997) revealed substructure in the X-ray map, but the resolution was not high enough to distinguish individual LMXBs.

The distance to NGC 1553 is somewhat poorly known, and reported values vary widely. However, NGC 1553 is known to be interacting with (and therefore at the same distance as) the elliptical galaxy NGC 1549. Consistent measurements for the distance to NGC 1549 of 24.2 Mpc are given by Faber et al. (1989; assuming $H_\circ = 50$ km s^{-1} Mpc^{-1}) and Tonry (2000) using the $D_n - \sigma$ and surface brightness fluctuations methods, respectively. We thus adopt 24.2 Mpc as the distance to NGC 1553.

2. OBSERVATION AND DATA REDUCTION

NGC 1553 was observed with *Chandra* on 2000 January 2-3 for a total of 33,882 s. The center of the galaxy was positioned on the ACIS-S3 CCD, with an offset of one arcmin from the nominal pointing for the S3. The S3 was selected for its sensitivity at low energies. In addition to the S3, data were received from the ACIS I2, I3, S2, and S4 CCDs. In the analysis that follows, we use data from the S3 chip only. The events were telemetered in Very Faint mode, the data were collected with frame times of 3.2 seconds, and the CCD temperature was -110 C. Only events with *ASCA* grades of 0,2,3,4, and 6 were included. Bad pixels, bad columns, and columns to either side of bad columns and node boundaries were excluded. Event PI values and photon energies were determined using the acisD1999-09-16gainN0004.fits gain file.

Chandra is known to experience periods of high background ("background flares"), which are particularly significant for the S3 chip (Markevitch 2000; Markevitch et al. 2000). We searched our data for such flares and found that, unfortunately, much of the exposure was affected by them. A light curve for the entire S3 chip for events with energies in the range 0.3 - 10.0 keV is displayed in Figure 1. There are 1000 time bins of 34.17 s. The average quiescent source plus background rate is about 1.19 ct s^{-1}, of which 0.85 ct s^{-1} are background (Markevitch 2000) and 0.34 ct s^{-1} are due to NGC 1553. The background flares are most prevalent during the first half of the exposure, where the background rate reached upwards of 60 ct s^{-1}. Ideally, one would like to remove all of the exposure where the background is increased significantly above the quiescent background (Markevitch 2000). Unfortunately, this would remove most of the exposure. In order to retain as much of the exposure as possible, while also keeping the signal-to-noise ratio as high as possible, we excluded data from our analysis that had a total S3 count rate greater than 5 ct s^{-1}. With this cutoff value, we eliminated 81% of the background and only 31% of the exposure. The resulting total exposure, corrected for background flares, is 23,192 s. We also searched for periods of incorrect aspect solution, and none were found.

In our analysis of the diffuse emission in NGC 1553, we determine the background from a circular region as far away as possible from the galaxy on the S3 CCD. Unfortunately, the elevated background in our observations, even after removing the strongest background flares, meant that we cannot use the available blank sky background fields, which were all taken during times of quiescent background only (Markevitch 2000). In addition, the other backside illuminated CCD (the S1) was turned off during this observation due to the FEP0 problem, so we could not take background from the S1. It is possible that even the outermost regions of the S3 chip may still contain some emission from NGC 1553, so our analysis may underestimate the total amount of diffuse emission. However, examination of the *ROSAT* PSPC image of NGC 1553 reveals that there does not appear to be galaxy emission in our background region. The analysis of resolved sources was not affected by this, as the background was determined locally so that both true background and superposed diffuse emission could be subtracted.

This observation was processed at a time when the standard pipeline processing introduced a boresight error of about $8''$ in the absolute positions of X-ray sources. We made an approximate correction for this error. The resulting position for the bright X-ray source near the center of NGC 1553 agreed with the *Hubble* Space Telescope (HST) position (data kindly provided by A. Kundu) of the center of the galaxy to $1.''9$. There are a number of arguments which indicate that the central X-ray source is associated with the active nucleus of the galaxy (§ 7.1). Thus, we corrected the X-ray positions so that the central X-ray source coincided with the nucleus of NGC 1553 as determined with HST. We also found a very good agreement ($0.''50$) between the positions of three X-ray sources and three globular clusters in NGC 1553 found with HST (A. Kundu, private communication). Before correction, all three globulars were displaced from their X-ray source in the same direction as the optical and X-ray position of the central AGN.

The initial data reduction was done with the *Chandra* analysis package CIAO. Some of the image analysis was done with IRAF/PROS. The spectra were extracted using software very kindly provided by Alexey Vikhlinin (Vikhlinin, Markevitch, & Murray 2000). The spectra were analyzed using XSPEC.

2.1. *X-ray Image*

Figure 2 shows the *Chandra* S3 image of NGC 1553 in the 0.3 - 10.0 keV energy band. The image has not been corrected for exposure or background. It has been smoothed slightly with a $\sigma = 0.''492$ (1 pixel) Gaussian so that features may be seen more easily. Discrete sources are evident and are concentrated at the center of the galaxy. The brightest source in the field is located at the center of NGC 1553, and is probably due to the active nucleus of the galaxy.

In addition, diffuse emission is apparent in Figure 2. In

general, the diffuse emission is elongated at a position angle of $\sim 140°$, which is similar to that of the optical light (Fig. 4 below). The diffuse component is seen more clearly in Figure 3 which displays the adaptively smoothed $4' \times 4'$ central region of the galaxy. The smoothed image has a minimum signal-to-noise ratio (SNR) of three per smoothing beam and was corrected for background and exposure. The grayscale is logarithmic and ranges from 3.8×10^{-7} to 3.0×10^{-3} ct pix^{-1} s^{-1}.

The diffuse X-ray emission is asymmetric with extensions to the NW and SE. In addition there is a bright "spiral" feature in the diffuse emission that runs SW to NE through the center of the galaxy. This spiral is approximately perpendicular to the optical axis.

3. RESOLVED SOURCES

Discrete sources were found on the ACIS S3 image by running the CIAO *wavdetect* wavelet detection algorithm. The source detection threshold was set at 10^{-6}, implying that $\lesssim 1$ false source (due to a statistical fluctuation) would be detected within the area of the S3 image. The detection limit for the sources corresponds approximately to a count rate of 4.3×10^{-4} ct s^{-1}. The sources were checked on the X-ray image, and the *wavdetect* count rates were verified with aperture photometry in IRAF/PROS. The count rates from the two methods agreed well in all cases. A total of 49 sources were found that exceeded the detection threshold; they are listed in Table 1. The columns give the source number, its name, its position, its projected distance d from the center of NGC 1553, the count rate and error, the signal-to-noise ratio SNR of the detection, the X-ray luminosity L_X assuming the sources are located at the distance of NGC 1553 (§ 4 below), and notes. The sources are listed in order of increasing distance from the center of NGC 1553. Based on background source number counts from the deep *Chandra* observations of Mushotzky et al. (2000) and Brandt et al. (2000), we expect that 6 - 12 of the sources in NGC 1553 may be unrelated to the galaxy.

We examined the positions of the resolved X-ray sources on the Digital Sky Survey (DSS) image of the field of NGC 1553. Figure 4 shows an overlay of the X-ray source positions onto the DSS image. We found six possible optical identifications from the DSS, which are noted with "DSS" in column 9 of Table 1. The DSS positions are consistently offset to the SW from the *Chandra* positions, with an average offset of $2''$. These associations are mainly in the outer parts of the field, as it is difficult to detect faint optical sources in the inner regions of NGC 1553 using the DSS.

We also compared the positions of our X-ray sources with a catalog of globular cluster candidates in NGC 1553 based on HST observations (A. Kundu, private communication). The three *Chandra* sources that have positions coincident (to within $0\farcs5$) with those of globular clusters are Srcs. 4, 11, and 23 (CXOU J041609.6-554642, CXOU J041611.0-554712, and CXOU J041621.5-554731). These sources are indicated by "HST" in the notes column. Based on the numbers of globular clusters and X-ray sources found within the region covered by the HST observation, we expect only 0.05 chance matches within $0\farcs5$. We therefore conclude that all three of these associations are probably real.

Comparison with the 843 MHz radio map in Harnett (1987) reveals extended radio emission with a flux density of 10 mJy coincident with the center of NGC 1553. In addition, there is a bright nearby point source with a flux density of 166 mJy at a distance of approximately two arcminutes from the galaxy center. The position of this radio sources coincides (within 1 arcsec) of the *Chandra* detected Src. 27, as well as an optical object on the DSS. It is likely a background object.

The second brightest resolved source detected on the S3 chip is Src. 38 which is more than an order of magnitude brighter than most of the other detected sources, and lies $3\farcm5$ to the SW of the center of the galaxy. It is coincident with an optical object on the DSS. This source was also seen in *BeppoSAX* data by Trinchieri et al. (2000), and over the course of their two observations, it varied in brightness. Given its distance from the center of the galaxy and its brightness, it is likely a background object. Trinchieri et al. (2000) also marginally detected a hard X-ray source (∼10–100 keV) with the PDS in the field of NGC 1553. The lack of spatial resolution of the PDS means that a counterpart could be anywhere within approximately 75 arcmin, which is much larger than the field of view of our *Chandra* observation. None of the *Chandra* sources has a hard X-ray flux (say, 5–10 keV) which is within an order of magnitude of the PDS source, so it is unlikely that this very hard X-ray emission is produced by any of the sources we detected.

3.1. *Hardness Ratios*

We first study the crude spectral properties of the resolved sources using hardness ratios, which have the advantage that they can be determined for fainter sources than detailed spectra. For consistency with the previous *Chandra* study of NGC 4697 (Sarazin, Irwin, & Bregman 2000), we use the three energy bands: soft S 0.3–1.0 keV, medium M 1.0–2.0 keV, and hard H 2.0–10.0 keV. As in Sarazin, Irwin, & Bregman (2000), we define two X-ray hardness ratios $H21 = (M - S)/(M + S)$, and $H31 = (H - S)/(H + S)$. For those resolved sources that have more than 20 counts, the hardness ratios and their errors are shown in Figure 5. For comparison, the hardnesses of the total emission (diffuse plus sources) are $H21 = -0.42$ and $H31 = -0.63$. Isolating the diffuse emission gives hardness ratios of $H21 = -0.60$ and $H31 = -0.81$, while the sum of the resolved sources yields $H21 = 0.12$ and $H31 = -0.07$. Most of the resolved X-ray sources have colors which are similar to the sources detected with *Chandra* in the X-ray faint elliptical NGC 4697 (Sarazin, Irwin, & Bregman 2000). Unlike NGC 4697, no supersoft sources were found.

The central source (Src. 1, CXOU J041610.5-554646), which is the brightest source in the field and whose position agrees with the nucleus of the galaxy, has hard X-ray colors, $H21 = 0.39$ and $H31 = 0.29$. This suggests that it is a strongly absorbed AGN rather than an X-ray binary in the galaxy (§ 7.1).

3.2. *Variability*

We searched for temporal variations in the X-ray emission from the individual resolved sources in the 0.3–10.0 keV energy band. We are limited in such searches by the

relatively small number of photons detected from most of the sources. The timing resolution is also limited by the frame time of 3.2 s. Thus, we only performed a relatively simple test; we used the Kolmogoroff-Smirov (KS) statistic to test the null hypothesis that the source plus background rate is uniform over the active exposure time. We consider sources to be possibly variable only if a uniform emission rate can be ruled out at the 90% confidence level. Using this technique, we find that five of the resolved sources may be variable. They are Srcs. 4, 17, 36, 40, & 41 (CXOU J041609.6-554642, CXOU J041602.9-554655, CXOU J041617.9-554955, CXOU J041545.5-554543, & CXOU J041611.5-555029), which have probabilities of 7.5%, 2.2%, 2.4%, 5.2%, and 4.6%, respectively, that they are not variable. The first of these sources is also coincident with a globular cluster candidate detected with HST. However, since we tested 49 sources, we expect 10% or ∼5 to appear to be variable due to random fluctuations.

4. LUMINOSITIES AND LUMINOSITY FUNCTION OF RESOLVED SOURCES

The count rates for the sources were converted into X-ray luminosities L_X in the 0.3–10.0 keV energy band assuming all of the sources are at the distance of NGC 1553 of 24.2 Mpc. To determine the conversion from count rate to unabsorbed energy flux in the band 0.3–10 keV, we used the best fitting spectral model for the cumulative spectrum of all of the resolved sources (excluding the central source and Src. 38 which is very bright and likely a background object). We fit the spectrum in the energy range 0.7–10.0 keV, where we are confident that the response is accurate, with a model including absorption fixed at the Galactic value, a soft blackbody component and a hard power-law component (§ 6.3). We then took the unabsorbed flux from 0.3–10.0 keV without refitting the spectrum for the expanded energy range. The resulting conversion between count rate and luminosity is 4.91×10^{41} ergs ct^{-1}. The luminosity values are given in column 8 of Table 1. The source luminosities range between 1.9×10^{38} and 1.8×10^{40} erg s^{-1}.

A luminosity function was constructed for the sources and is plotted as a histogram in Figure 6. The central source (Src. 1) was not included in this luminosity function. We fit the luminosity function of the resolved sources to either a power-law or broken power-law model for the galactic sources, plus the expected contribution of background and foreground sources, determined from the deep blank field *Chandra* observations of Brandt et al. (2000) and Mushotzky et al. (2000). The background sources are assumed to follow the number versus flux relation derived from *ROSAT* deep fields (Hasinger et al. 1998). A single power-law did not produce an acceptable fit to the observed luminosity function; it could be rejected at the >94% confidence level. Fitting a broken power-law, however, resulted in a good fit, which is shown as the continuous curve in Figure 6. The broken power-law luminosity function takes the form:

$$\frac{dN}{dL_{38}} = N_\circ \left(\frac{L_{38}}{L_b} \right)^{-\alpha}, \qquad (1)$$

where $\alpha = \alpha_l$ for $L_{38} \leq L_b$, $\alpha = \alpha_h$ for $L_{38} > L_b$, and L_{38} is the 0.3–10 keV X-ray luminosity in units of 10^{38} erg s^{-1}. The best fit, determined by the maximum-likelihood method, with errors determined with Monte Carlo simulations, gave $N_\circ = 8.7^{+10.4}_{-3.5}$, $\alpha_l = -0.1^{+1.2}_{-4.3}$, $\alpha_h = 2.7^{+0.7}_{-0.4}$, and a break luminosity of $L_b = 4.1^{+1.6}_{-1.1} \times 10^{38}$ erg s^{-1}. Because of the limited range of luminosities observed below the break luminosity, the low luminosity slope α_l is very poorly determined.

To examine how incompleteness might affect the luminosity function at the faint end, we simulated the observation using MARX (Model of AXAF Response to X-rays; Wise et al. 2000), version 3.01. We assumed that the luminosity function of the sources was a single continuous power-law, which matched the best-fit NGC 1553 luminosity function above L_b. This power-law was continued to a low luminosity at which the total LMXB luminosity matched the observed total (resolved and unresolved) LMXB emission in NGC 1553. The diffuse emission and background were modeled based on a wavelet reconstruction of the unresolved emission in NGC 1553, corrected for unresolved LMXBs. The sources in the simulated observation were detected using WAVDETECT using the same criteria as in the real data, and their count rates were converted into luminosities in the same way as the real sources. We found that the luminosity function of the simulated sources was depressed below the input model luminosity function below a luminosity of approximately 2×10^{38} erg s^{-1}. While this is below the break luminosity determined from the data in NGC 1553, it shows that incompleteness strongly affects the slope of the luminosity function below the break luminosity. Given the large statistical errors in α_l and the substantial systematic effect of incompleteness, we believe the value of α_l is unreliable. Based on the simulation, we do not believe that the break in the observed luminosity function at $L_b = 4.1 \times 10^{38}$ erg s^{-1} is due to incompleteness; however, the systematic uncertainty due to incompleteness increases the total errors in L_b to about a factor of two.

The break luminosity measured for NGC 1553 is about twice the Eddington luminosity for spherical accretion of hydrogen dominated gas onto a 1.4 $M_\odot$ neutron star. Therefore, it may be that the sources with luminosities much higher than the break are accreting black holes, and those below the break are predominately neutron stars in binary systems.

A broken power-law was also used to fit the luminosity function of the sources derived from *Chandra* data of NGC 4697 (Sarazin, Irwin, & Bregman 2000). The break luminosity found for this galaxy ($L_b = 3.2^{+2.0}_{-0.8} \times 10^{38}$ erg s^{-1}) is similar to that of NGC 1553. The fit to NGC 4697, scaled by the optical luminosity (NGC 1553 is 2.04 times brighter than NGC 4697 in the B-band) is shown as a dashed line plotted over the luminosity function in Figure 6. The cumulative luminosity function of NGC 1553 is higher at the bright end, and lower at the faint end. At the bright end, the two luminosity functions agree within the errors, including the systematic error in the number of background sources. At the faint end, they disagree significantly. This is certainly due, at least in part, to incompleteness in the luminosity function of NGC 1553 at the faint end. The luminosity limit for the NGC 4697 observation is about a factor of four fainter than in NGC 1553.

We determined the $L_{X,src}/L_B$ ratio for NGC 1553,

where $L_{X,src}$ is the X-ray luminosity in the $0.3-10.0$ keV band for the resolved and estimated unresolved sources within two effective radii, and L_B is the B-band luminosity within two effective radii. We find a $L_{X,src}/L_B$ value of 7.2×10^{29} erg s^{-1} $L_{\odot,B}^{-1}$, which is slightly lower than the value found for NGC 4697 of 8.1×10^{29} erg s^{-1} $L_{\odot,B}^{-1}$, The unresolved source contribution to $L_{X,src}$ was estimated assuming that 24% of the diffuse counts derive from unresolved sources (see §5), based on counts in different energy bands and spectral fits. For NGC 1553, $L_{X,src}$ is dominated by the unresolved sources, and its accuracy is therefore limited by how well we can estimate the contribution to the diffuse emission from the unresolved sources.

Another question is whether the number, or total luminosity, of LMXBs scales with the optical luminosity of the galaxy. Given that LMXBs represent an old stellar population, it might be that they scale with the bulge luminosity, rather than the total luminosity, in S0 galaxies. An even more intriguing idea is that all or most LMXBs may have formed in globular clusters (White, Kulkarni, & Sarazin 2001). Thus, the number of LMXBs may scale with the number or total luminosity of globular clusters. Scaling either with the bulge luminosity or population of globular clusters would lower the expected number of fainter LMXBs in NGC 1553 relative to NGC 4697, and might explain the observed difference in their $L_{X,src}/L_B$ ratios.

5. RESOLVED VERSUS DIFFUSE EMISSION

We have determined the relative contributions of resolved sources and diffuse emission to the total counts within an elliptical region defined by two effective radii. One effective radius defines the elliptical optical isophote containing one half of the optical light; this isophote has a semi-major axis of 78″, an ellipticity of 0.345, and is at a position angle $PA = 149°.5$ (Kormendy 1984; Jorgensen, Franx, & Kjaergaard 1995). The two effective radii elliptical region (semi-major axis of 156″) contains all of the emission shown in Figure 3. In the energy band of 0.3–10.0 keV, the X-ray emission is dominated by the diffuse component, which makes up 70% of the counts. The remaining 30% of the emission is from the resolved sources, which are presumably X-ray binaries. In the soft S band (0.3–1.0 keV), 84% of the detected emission is diffuse, and the remaining 16% is due to resolved sources. In the medium M (1.0–2.0 keV) and hard H (2.0–10.0 keV) bands, the fractions are 51% diffuse and 49% resolved and 39% diffuse and 61% resolved, respectively. Thus, the diffuse emission is rather soft, while the resolved sources dominate the hard X-ray band.

The diffuse component is much softer than the discrete sources (see § 6), consistent with it being composed at least partly of hot gas rather than only unresolved X-ray binaries. Based on the counts from the diffuse component in the soft (0.3–1.0 keV), medium (1.0–2.0 keV), and hard (2.0–10.0 keV) bands we estimate that 28% of the diffuse counts are from unresolved X-ray binaries. This assumes that the X-ray binaries make up all of the hard counts. Comparing the hard and soft components of the best fit model to the spectrum of the diffuse emission (§ 6.2), we estimate that hard emission makes up 20% of the counts in the 0.3-10 keV band. From these two methods, then, we estimate that 24±4% of the diffuse counts are a result of unresolved X-ray binaries.

Using the best-fit spectral models for the total emission, resolved sources, and diffuse emission (§ 6), we determined the unabsorbed flux and luminosity of each of these components in the band 0.3–10.0 keV. For the region within two effective radii, the total flux is 1.43×10^{-12} erg cm^{-2} s^{-1}. The total flux from all of the resolved sources, including the bright central source, within this region is 5.80×10^{-13} erg cm^{-2} s^{-1}. Subtracting the two gives the diffuse flux within two effective radii of 8.45×10^{-13} erg cm^{-2} s^{-1}. For deriving the fluxes, note that the spectrum fitted for the sum of the sources includes the central object and includes the objects within two effective radii only. This is so that this flux can be subtracted from the total flux to give directly the flux of the diffuse emission. To more carefully examine the spectrum of the sources in more detail, in (§ 6), we sum the sources from the entire S3 chip to increase the number of counts in the spectrum, and we exclude the central object and object #38 in an attempt to include only LMXBs in the spectrum. Converting the fluxes to luminosities using a distance to NGC 1553 of 24.2 Mpc gives $L_X = 1.00\times10^{41}$ erg s^{-1} for the total emission, $L_X = 4.08\times10^{40}$ erg s^{-1} for the sum of the sources, and $L_X = 5.94\times10^{40}$ erg s^{-1} for the diffuse emission, all within two effective radii and for the 0.3 - 10.0 keV energy band. The fluxes are all affected by the uncertainty of *Chandra*'s response at low energies (below 0.7 keV). The flux for the diffuse component is most uncertain because its spectrum is dominated by soft emission.

6. X-RAY SPECTRA

We used the software package kindly provided by Alexey Vikhlinin (Vikhlinin et al. 2000) to extract spectra and to determine the response matrices. The response matrices were determined from the FITS Embedded Function (FEF) response files FP-110_D1999-09-16fef_piN0002, appropriate to the operating temperature of -110 C. The areas of the detector were weighted by the extracted counts in determining the response matrices. For the resolved sources, background spectra were extracted from local regions around each of the sources. For the total spectrum or the spectrum of the diffuse emission, we used a background region as far as possible from NGC 1553 but on the S3 chip (§ 2). Because the soft X-ray spectral response of the S3 chip was poorly known at the time when this analysis was done, we restricted our spectral analysis to the energy range 0.7–10.0 keV. In order to allow χ^2 statistics to be used, all of the spectra were grouped to at least 20 counts per spectral bin. Models were fit to the spectra using XSPEC. The results are summarized in Table 2, where the errors are at the 90% confidence level.

Previous *ROSAT* and *ASCA* spectra of early-type galaxies have indicated that they have at least two spectral components, a very hard component which may be due to X-ray binaries and/or an AGN (Matsumoto et al. 1997; Allen et al. 2000), and a softer component. In X-ray luminous early-type galaxies, the soft component is dominant, and it is clearly due to diffuse gas at a temperature of ∼1 keV (Forman, Jones, & Tucker 1985; Canizares, Fabbiano, & Trinchieri 1987). In X-ray faint early-type galaxies, the soft component is much softer, and its origin is still uncertain (Fabbiano, Kim, & Trinchieri 1994; Pellegrini 1994; Kim et al. 1996; Irwin & Sarazin 1998a,b).

The *ASCA* spectrum of the hard component has generally been fit by either a power-law (characterized by a photon spectral index Γ, where $\Gamma > 0$ implies a photon spectrum which declines with energy) (Allen et al. 2000) or by a thermal bremsstrahlung spectrum (characterized by a hard component temperature T_h; Matsumoto et al. 1997). The soft component in X-ray bright galaxies is usually fit by the Raymond-Smith (Raymond & Smith 1977) or MEKAL model for the emission from a low density, optically thin plasma (Fabbiano et al. 1994). This model is characterized by the temperature of the gas (T_s) and by the abundances of the heavy elements. Given the limited statistics we have in our spectra, we will assume that the heavy element abundances have the solar ratios, and only allow the overall abundance of the heavy elements to vary. In X-ray faint galaxies, it is unclear what the appropriate soft emission model should be. If the soft emission is due to diffuse gas, then the MEKAL model would again be appropriate. If it is due to an optically thick stellar component (including the same LMXBs which produce the hard component), then it might be better represented as a blackbody, characterized by a temperature (T_s again). Thus, we have used spectral models which include both a hard (power-law or bremsstrahlung) and soft (MEKAL or blackbody) component.

6.1. *Total X-ray Spectrum*

We first determined the total spectrum (resolved sources and diffuse emission) from within two effective radii. The spectrum is shown in Figure 7. We tried fitting the spectrum with either a pure hard component (power-law or bremsstrahlung) or a pure soft component (MEKAL or blackbody), but they did not provide an adequate fit. We allowed the absorbing column N_H to vary, and found that the fit was not significantly improved ($\Delta\chi^2 < 1$) over using the Galactic column towards NGC 1553 of 1.41×10^{20} cm^{-2} (Dickey & Lockman 1990). We therefore fixed the absorption to the Galactic value.

When the hard component is modeled by thermal bremsstrahlung, the temperature diverges and is unconstrained (XSPEC imposes a limit of $kT_h \leq 200$ keV). At such high temperatures, the shape of thermal bremsstrahlung at lower energies resembles a power-law with a photon index of $\Gamma \approx 1.4$. This suggests that a power-law might provide a better fit for the hard component. Indeed this is found to be the case, although the improvement is not very substantial. We list two fits in Table 2, one with the photon index a free parameter, and the other with it fixed to the value found from fitting the sources (§6.3) of $\Gamma = 1.20$ since we expect that it is discrete sources that make up the hard component. The fit with the free photon index is better in the 0.7–10.0 keV range, however, when we expand the energy range to 0.3–10.0 keV and do not refit the model, the fit with the fixed photon index is much better. Therefore, we use the model with the fixed photon index when determining the flux and luminosity in the 0.3–10.0 keV range (the same is true for the diffuse, spiral, and circle components described below).

We tried to fit the soft component with a MEKAL, blackbody (bbody) or disk blackbody (diskbb) model. The MEKAL model provided the best fit. The temperature of the cooler component was ∼0.47 keV, and the abundance was ∼0.16. This temperature is consistent with that determined from the temperature vs. velocity dispersion ($kT - \sigma$) correlation derived from *ROSAT* observations of elliptical galaxies (Davis & White 1996), using a velocity dispersion for NGC 1553 of $\sigma = 184$ km s^{-1} (Longo et al. 1994). The abundance is consistent with the temperature-abundance relation reported by Davis & White (1996), who found that abundance increases as temperature increases. The spectrum in the 0.7–10.0 keV range is displayed in Figure 7 with the model including absorption fixed at the Galactic value, a MEKAL component, and a power-law with the photon index set to 1.20. The observed spectrum clearly shows the (mainly) Fe XVII (∼0.72 keV emitted), Fe XVII (0.826 keV emitted), and the Ne X, Fe XVII, Fe XXI (∼1.02 keV) line complexes, indicating that a significant portion of the soft emission is thermal emission from gas. For this fit the luminosities of the hard and soft components are $L_{X,h} = 7.79 \times 10^{40}$ erg s^{-1} and $L_{X,s} = 2.23 \times 10^{40}$ erg s^{-1}, respectively, giving a ratio $L_{X,h}/L_{X,s} = 3.45$. The ratio of the hard-to-soft model count rates is 0.99.

We simultaneously fit the *Chandra* spectrum of the total emission with a spectrum extracted from an identical region in the *ROSAT* PSPC using a model combining MEKAL and power-law components. The resulting fit agreed with the fits to the total emission described in Table 2 within the errors.

Trinchieri et al. (2000) fit a two-component model to a spectrum derived from *BeppoSAX* MECS and LECS data of NGC 1553. Using a Raymond-Smith model, they found a lower temperature ($kT = 0.26$ keV) for the soft component, although the two measurements overlap within the errors. The LECS is sensitive to lower energies (down to 0.1 keV) than our cutoff of 0.7 keV, and sampling this low energy range has a significant effect on determining the temperature of the soft emission. In addition, Trinchieri et al. extracted their spectrum from a larger spatial region than we did. If there is a negative temperature gradient, we would expect the average temperature derived from the spectrum from this larger region to be lower. Trinchieri et al. used a thermal bremsstrahlung model to fit the hard emission component. They found a temperature of 4.8 keV for the hard component which therefore has a steeper decline with photon energy than we found.

6.2. *Diffuse X-ray Spectrum*

We extracted the spectrum of the diffuse emission (excluding the resolved sources) from within two effective radii. Again, we tried fitting several models. The best fit model required both a soft MEKAL component and a hard power-law component. This fit is better than a fit of just a soft component at the 99.93% confidence level, and better than the fit of a hard component model at the 99.99% level. The absorption was set to the Galactic value since freeing it did not improve the fit. Two fits are listed in Table 2, one with the photon index allowed to vary and one with it fixed to the source value of $\Gamma = 1.20$. As with the total emission, the fit is better in the 0.7–10.0 keV range when the photon index is free. Expanding the energy range to 0.3–10.0 keV without refitting the model shows that the model with the fixed photon index is much better at low energies.

The spectrum of the diffuse component is shown in Figure 8, along with a solid line representing a model includ-

ing Galactic absorption, MEKAL emission, and a power-law with the photon index fixed to the source value. The ratio of the hard-to-soft model count rates is 0.26. The ratio of the luminosities of the hard to soft components in the diffuse emission is $L_{X,h}/L_{X,s} = 0.88$, which is smaller than the value for the total emission ($L_{X,h}/L_{X,s} = 3.45$), or the resolved sources ($L_{X,h}/L_{X,s} = 6.85$, see below). Thus, the diffuse emission is mainly soft X-rays. The soft spectrum and the good fit to a MEKAL model suggest that much of the soft emission is due to diffuse gas. As was true to the total spectrum, the diffuse spectrum shows the (mainly) Fe XVII (∼0.72 keV emitted), Fe XVII (0.826 keV emitted), and the Ne X, Fe XVII, Fe XXI (∼1.02 keV) line complexes, which supports the predominance of thermal emission due to hot gas. The hard component in the diffuse emission may be due to unresolved LMXBs below the limit of detection as discrete sources.

6.3. *X-ray Spectrum of Resolved Sources*

We determined the spectrum of the sum of all of the resolved sources on the S3 chip, excluding the central source and source #38. Src. 38 is likely an unrelated background source and we therefore exclude it when extracting the spectrum of the sum of the sources. Several pieces of evidence point towards the central source being an AGN rather than an LMXB like most of the other discrete sources, so we analyze its spectrum separately in § 6.4.

We achieved the best fit to the spectrum by using a model combining a soft, blackbody component, and a hard, power-law component. The f-test showed that the fit including both a soft and hard component was better than a fit with just a hard, power-law component at a significance level of 96%. When a MEKAL model was used for the soft component, the abundance and temperature were very poorly determined, and there is no real evidence for line emission in the spectrum. Thus, we also fit the soft component with a blackbody spectrum which gave an acceptable fit. The fit was not improved by allowing the absorption to vary so we set it to the Galactic value. The spectrum is shown in Figure 9, along with the fit of a model combining absorption set to the Galactic value, blackbody emission, and a power-law component. The best fitting model gave a blackbody temperature of $kT_s = 0.24$ keV and a power-law photon index of $\Gamma = 1.20$.

The resolved sources have a harder spectrum than that of the diffuse emission. The ratio of the hard-to-soft model count rates is 2.08. The luminosities of the hard and soft components, excluding the central source and Src. 38, are $L_{X,h} = 2.35 \times 10^{40}$ erg s^{-1} and $L_{X,s} = 3.43 \times 10^{39}$ erg s^{-1}, respectively, giving a ratio of $L_{X,h}/L_{X,s} = 6.85$.

6.4. *X-ray Spectrum of Central Source*

We determined the X-ray spectrum of the central X-ray source, which is the brightest source in the field. The spectrum and best fit model are shown in Figure 10. This spectrum is best fitted with a disk blackbody model with a temperature of $kT = 1.70$ keV and a high absorbing column ($18.25^{+7.42}_{-7.59} \times 10^{20}$ cm^{-2}), much higher than Galactic. This hard, absorbed spectrum is consistent with the hardness ratios of this source (§ 3.1). This spectrum indicates that the central source is different than most of the other resolved sources, which are presumably LMXBs. The hard spectrum and high absorption suggest that this source is an obscured AGN. The disk blackbody model provides a better fit than a power-law model at the 66% level as shown by the f-test. The power-law model has a best-fitting photon index of $\Gamma = 1.59$, and a high absorbing column of $36.04^{+12.96}_{-9.22} \times 10^{20}$ cm^{-2}). This photon index is consistent with that seen for Weak Line Radio Galaxies and LINERs (e.g., Sambruna et al. 1999).

6.5. *X-ray Spectrum of Spiral Feature*

In order to study the origin of the spiral feature seen in the diffuse emission (Figs. 2, 3), we determined its spectrum. A spatial region was constructed which covered the feature as seen in Figure 3, but excluding the central source and other resolved sources. In order to compare this feature with the surrounding diffuse emission, we also extracted the spectrum for a circular region centered on the galaxy that just enclosed the spiral region, and excluded the spiral region and discrete sources found within the circle.

Best fitting models to the spiral and circular regions are listed in Table 2. As above, letting the absorption vary did not improve the fits, so we set it to its Galactic value. When the photon indices are allowed to vary, the spiral component has a best fitting power-law that is inverted with $\Gamma = -1.55$. Examination of the spectrum indicates that there is excess hard emission coming from the spiral region. This emission probably also affects the fits to the total and diffuse components which both include the spiral region and also have best fitting power-laws with low or negative photon indices. The circular region which excludes the spiral emission has a photon index consistent with that of the sources. The high abundance indicated by the fit of the spiral component with the photon index fixed to the source value is the result of trying to fit the lines at high energies where the model continuum is lower than in the fit with the inverted power-law. This high abundance, therefore, is most likely not real. The abundance measured with the fit using the free photon index is consistent with the abundance measured for the circular, total, and diffuse regions. The excess hard emission in the spiral region may be non-thermal, inverse Compton radiation resulting from a shock. A high-resolution radio map would be useful in determining more definitively the origin of this emission.

7. DISCUSSION

7.1. *Nature of the Central Source*

In principle, the central X-ray source in NGC 1553 might be due to one or several LMXBs and/or to a central AGN. However, previous observations in other wavebands indicate that it is an AGN, and our X-ray observations support this picture. NGC 1553 is a weak radio source (10 mJy at 843 MHz; Harnett 1987), with a LINER-like optical emission spectrum (Phillips et al. 1986). The X-ray evidence that suggests the central source is an AGN follows. First, the position of this source agrees with the position of the optical nucleus of the galaxy to within the errors. Second, its luminosity is $L_X = 1.75 \times 10^{40}$ erg s^{-1}, which would make it an extremely luminous X-ray binary. This luminosity corresponds to the Eddington limit for spherical accretion by a ≈130 $M_\odot$ compact object. While such

luminous, high mass, presumably black hole binaries may have been found in star formation regions in spiral galaxies (e.g., Kaaret et al. 2000), it seems unlikely that they would occur in LMXBs.

Third, the central source has a harder X-ray spectrum than is typical of the other resolved sources in this galaxy, as shown both by its hardness ratios (§ 3.1) and its detailed X-ray spectrum (§ 6.4). The X-ray spectrum has very strong soft X-ray absorption, which is completely inconsistent with Galactic column in this direction (Table 2). The X-ray spectrum is consistent with that expected for an obscured AGN, surrounded by a significant column of nuclear gas.

7.2. *Relation of Diffuse Emission Features to Cooler Gas*

In addition to the hot, X-ray emitting gas, NGC 1553 contains cooler gas seen in optical emission lines and as dust extinction features (Phillips et al. 1986; Bettoni & Buson 1987; Bally & Thronson 1989; Roberts et al. 1991; Trinchieri et al. 1997; Quillen et al. 2000). Based on a lower spatial resolution *ROSAT* HRI X-ray image, Trinchieri et al. (1997) argued for an association of a region SE of the nucleus of NGC 1553 seen in Hα emission with a region of enhanced X-ray emission. The X-ray region noted by Trinchieri et al. is apparently the extension to the SE in Figure 3. We agree with this association of the X-ray emission with Hα emission. On the other hand, there is no corresponding Hα feature associated with the extension to the NW, and, on smaller scales near the center of the galaxy, Hα emission is not aligned with the "spiral feature." A north-south dust lane, approximately $3''$ across, is seen with HST at the center of the galaxy (Quillen et al. 2000). It runs approximately perpendicular to the spiral region, and has no correlation with any of the X-ray emission features. The position angle of the dust lane seems to approximately agree with that of small-scale Hα emission at the center of the galaxy (Trinchieri et al. 1997). Overall, there isn't much evidence for a strong correlation of the X-ray morphology with cooler gas and dust.

7.3. *Origin of the Spiral Feature*

We now consider the origin of the "spiral feature" seen in X-rays near the center of NGC 1553 (Figs. 2 & 3). The hardness ratios, or "colors" for these regions are indistinguishable from those of the diffuse emission as a whole, and the emission is predominately soft (approximately 70% of the counts fall in the 0.3–1.0 keV energy band). Spectral fits (§ 6.5) show that the gas forming the spiral feature has approximately the same temperature, abundance, and absorbing column as the surrounding gas. We also determined the average X-ray surface brightness enhancement of the spiral feature compared to the surrounding diffuse emission, using a number of regions to collect counts from the feature and from a circular region which just enclosed it. In the 0.3–10 keV band, the spiral feature has an average surface brightness enhancement of 1.82 compared with the emission immediately surrounding it. We converted this surface brightness contrast into a density contrast, assuming the best-fit spectra for the spiral and surrounding gas, and for two simple geometries. First, we assume that the extent of the spiral feature along the line of sight is comparable to its width (e.g., it is a narrow filament) on the plane of the sky (an angle of approximately 35°). In this case, the spiral gas is denser than the surrounding material by an average factor of $\rho_{sp}/\rho = 1.87$. As an alternative, we assume that the extent of the spiral feature along the line of sight is comparable to the distance from the nucleus of the galaxy (e.g., it is a sheet of enhanced emission). This sheet geometry may require that we are observing the system at a preferred angle (along the sheet), or that it be part of a limb-brightened structure. For this geometry, the density contrast of spiral gas is an average factor of about $\rho_{sp}/\rho = 1.35$.

First, we consider the possibility that this feature is due to absorption; that is, the spiral is not an emission feature, but the result of excess absorption in the surrounding region. In fact, the spectral fits indicate that there is not enough excess absorption in the surrounding region to provide a significant surface brightness enhancement for the spiral. Also, if the required excess absorption were due to cooler gas, one might expect the spiral feature to be surrounded by optical emission lines or dust absorption; neither is the case (§ 7.2). It also seems improbable that absorption in the surrounding gas would produce such a well defined spiral feature.

Second, X-ray enhancements might be due to the interaction between hot X-ray emitting gas and cooling material, leading to the evaporation of the cooler material (Kim 1989; Sparks, Macchetto, & Golombek 1989; Macchetto et al. 1996; Sparks 1997). This model for the spiral feature would require that there be a very close association with optical emission line gas and/or dust. As noted above (§ 7.2), no such association is seen in NGC 1553.

Third, the spiral features might be tidal in origin. In support of this idea, we note that NGC 1553 is interacting with the companion elliptical galaxy NGC 1549. There are shell or tidal features seen in NGC 1553 (Malin & Carter 1983; Bridges & Hanes 1990), but all are at large radii. There are no distortions apparent in the HST optical image of NGC 1553 which are associated with the spiral feature, or which are located at similar radii. If the spiral feature was due to gravitational tides, one would expect the stars to show a similar effect.

Fourth, the spiral might be due to gas which is radiatively cooling, and then being sheared as a result of slow rotation. In X-ray bright early-type galaxies, the cooling time is short in the central regions, and the gas is believed to form a cooling flow (e.g., Sarazin 1990). We estimate the radiative cooling time of gas in the spiral region. Using the peak surface brightness of the spiral region of 7.5×10^{-6} ct pixel^{-1} s^{-1}, along with the best fitting spectral model, we determine the approximate density of this region for both the filamentary and sheet-like geometries. For the filamentary (sheet) geometry, we estimate the density corresponding to the peak in surface brightness as $n_e = 0.026$ (0.019) cm^{-3}. The isobaric cooling time is then $t_{cool} \approx 1.5$ (2.0) $\times 10^8$ yr for the filamentary (sheet) geometry. This is much shorter than the probable age of the system, so it is likely that the gas in the spiral is cooling, unless some other source of energy is replacing the radiative losses.

In this case, we would expect the gas in the spiral feature to be cooler than the surrounding gas. The spiral component has a best fitting MEKAL temperature of $0.51^{+0.07}_{-0.08}$

keV and that of the circular region is $0.48^{+0.07}_{-0.09}$ keV. The ratio of the temperature in the spiral region to the temperature of the surrounding region is then $T_{sp}/T = 1.05^{+0.23}_{-0.23}$ at a 90% confidence level. Obviously, this doesn't rule out the spiral gas being cooler than the ambient gas. On the other hand, the radiative cooling time is much longer than the dynamical time for the gas, $t_{dyn} \approx 10^7$. Thus, one would expect the cooling gas to be nearly in pressure equilibrium with the surrounding. If we take the lower limit of the temperature contrast of $T_{sp}/T > 0.81$, and use density contrasts derived above, we find a minimum pressure ratio of $P_s/P > 1.10$ for the long (sheet) geometry and $P_s/P > 1.52$ for the narrow (filament) geometry. Other sources of pressure support, such as magnetic fields, would only increase this limit further. Thus, it seems unlikely that the gas in the spiral feature in in pressure equilibrium.

Another concern is the large contrast between the cooling time and the dynamical time in the gas. It seems unlikely that the spiral structure could be maintained while the gas cooled. This would probably require a very small but nonzero rotation and some other mechanism, such as magnetic fields, to stabilize the cool gas regions against infall or being sheared away. It is also difficult to understand why the feature would be two armed and relatively symmetric if it were due to radiative cooling of random perturbations in the ambient gas. The sum of the evidence suggests that it is unlikely that the spiral feature is due to cooling.

Next, we consider the possibility that the spiral region is due to adiabatic compression; If we ignore magnetic fields or other pressure sources, adiabatic compression requires that $T_{sp}/T = (\rho_{sp}/\rho)^{2/3}$. For the density contrast associated with a filamentary (sheet-like) geometry, this implies a temperature contrast of $T_{sp}/T = 1.52$ (1.22). The observed temperature contrast is consistent with adiabatic compression for a sheet-like geometry, but not for the filamentary geometry.

Finally, we consider the possibility that the spiral features are shocks. Again, we assume an ideal gas, with no magnetic fields or other sources of pressure. Then, the temperature increase T_{sp}/T and shock compression $r \equiv \rho_s/\rho$ are related by (Markevitch, Sarazin, & Vikhlinin 1999)

$$\frac{1}{r} = \left[\frac{1}{4}\left(\frac{\gamma+1}{\gamma-1}\right)^2\left(\frac{T_{sp}}{T}-1\right)^2 + \frac{T_{sp}}{T}\right]^{1/2} - \frac{1}{2}\frac{\gamma+1}{\gamma-1}\left(\frac{T_{sp}}{T}-1\right), \qquad (2)$$

with $\gamma = 5/3$. From the spectrally-derived upper limit on the temperature contrast of $T_{sp}/T < 1.282$, we find an upper limit to the compression $r = \rho_{sp}/\rho < 1.427$. Therefore, a simple shock model using a sheet-like geometry can explain the increase in surface brightness, although a filamentary geometry cannot. The velocity discontinuity Δu_{sh} at the shock is given by (Markevitch et al. 1999)

$$\Delta u_{sh} = \left[\frac{kT}{\mu m_p}(r-1)\left(\frac{T_{sp}}{T}-\frac{1}{r}\right),\right]^{1/2}, \qquad (3)$$

where $\mu = 0.61$ is the mean mass per particle in terms of the mass of the proton m_p. For the upper limit temperature increase, the velocity change at the shock is $\Delta u_{sh} < 138$ km s^{-1}, and the shock velocity relative to the ambient gas is $u_{sh} = \Delta v_{sh} r/(r-1) < 462$ km s^{-1}.

Thus, it seems most likely that the spiral feature results from subsonic or moderately transonic compression of the ambient gas in the region. The gas is required to be in a sheet rather than a filament. The required velocities are comparable to orbital velocities in the galaxy, so it is possible that the spiral feature is a shell, similar to the stellar dynamical shell seen in the optical in the outer part of NGC 1553.

On the other hand, the spiral feature might be a part of a limb-brightened shell of gas compressed by expanding radio lobes from the radio nucleus (Harnett 1987). Since the lifetimes of radio sources (typically, $\lesssim 10^7$ yr) are shorter than the cooling time of the gas, this model can explain why the gas has been compressed without significant radiative cooling. Similar shells have been seen in several cooling flow cluster central galaxies (McNamara et al. 2000; Fabian et al. 2000). This would explain the nearly symmetric geometry (i.e., why it is present on both sides of the nucleus). The required radio jets and lobes would extended in a direction perpendicular to the dust and Hα disk near the center of the galaxy (Trinchieri et al. 1997; Quillen et al. 2000). The geometry has been seen in other radio galaxies (e.g., McNamara et al. 2000), and is consistent with the dust lane being the outer portion of an accretion torus around the AGN, with the radio jets emerging along the rotation axis of the torus. This model predicts that the spirals form as rims around the radio source, which must have a double jet/lobe structure. The S-shaped X-ray structure may indicate that the radio jets are not propagating along a symmetry axis of the galaxy, as it also required if the jets are perpendicular to the dust lane. In this case, each of the jets would encounter denser gas on one side, and an S-shaped structure would be produced.

Unfortunately, we have been unable to find a radio image of this southern galaxy which resolves the galaxy. The only information available is the approximate flux density of 10 mJy at 843 MHz (Harnett 1987). Upper limits at higher frequencies do not usefully limit the radio spectral index. There are several other published radio flux densities for this galaxy, however, as revealed by the Harnett (1987) map, they include an unrelated bright neighboring source in the flux density measurements. The radio source associated with the nucleus of NGC 1553 is rather faint, and may be too weak to affect the hot interstellar gas in NGC 1553 enough to produce the spiral features. To test very crudely this idea, we assume that the radio source has displaced two spherical regions of thermal gas, each with a diameter of 30″. We assume that the minimum pressure in the radio source is the estimated thermal pressure in the spiral feature assuming the "sheet" geometry, $P_{sp} \approx 3 \times 10^{-11}$ dynes cm^{-2}. Then, the minimum total energy content of the two radio lobes is $E_{radio} \gtrsim 6 \times 10^{55}$ ergs. The radio power at a frequency of $\nu = 847$ MHz is $P_\nu \approx 7 \times 10^{20}$ W Hz^{-1}. If we assume that the radio spectrum is a power-law $P_\nu \propto \nu^\alpha$ extending from 0.01 to 100 GHz, then the total luminosity is $L_{radio} \approx (5-11) \times 10^{37}$ ergs s^{-1} for $-1.5 < \alpha < -0.7$. We assume that the radio source is powered by a jet, and that the efficiency of conversion of jet power L_{jet} into radio luminosity is ϵ_{jet}, so that

$L_{jet} \approx (5-11) \times 10^{39} (\epsilon_{jet}/0.01)^{-1}$ ergs s^{-1}. In order to inflate the required cavities, this jet would have to operate for a time scale of $t_{radio} \approx E_{radio}/L_{jet} \gtrsim 2 \times 10^8 (\epsilon_{jet}/0.01)$ yr. This is somewhat longer than the ages usually assumed for radio sources, so either the jet efficiency would need to be unusually low, or the radio source is presently weak but was stronger in the recent past.

As a alternative test of the radio interaction hypothesis for the spiral feature, we assume that the observed radio flux comes from the two radio cavities needed to produce the structure, and determine the minimum energy content of these lobes. In addition to the previous assumptions, we assume that the magnetic field is perpendicular to the line of sight and that the ratio of energy in ions to electrons in the radio lobes is unity. Since the radio spectral index is unknown, we allow it to vary and require that the minimum radio source energy exceed that required to inflate the cavities. This requires that $\alpha \lesssim -2.7$, which is an extremely steep spectrum. Instead, if we assume the ratio of ions to electrons is 100, the limit is $\alpha \lesssim -1.7$. These results indicate that the radio source can explain the spiral feature only if it is far from the minimum energy or equipartition limit. Both of these arguments suggest that the spiral feature can be explained by an interaction with the radio source only if the radio source is a fading remnant of previously more intense radio activity.

8. CONCLUSIONS

Using a *Chandra* observation of the X-ray faint S0 galaxy NGC 1553, we have spatially and spectrally resolved the sources of its X-ray emission. A significant fraction, approximately 70%, of the total X-ray counts in the 0.3–10.0 keV band are detected as diffuse emission and 49 discrete sources are resolved. The diffuse emission dominates at soft energies, making up 84% of the counts from 0.3–1.0 keV, while the resolved sources make up most of the hard emission with 61% of the counts in the 2.0–10.0 keV band. We estimate that approximately 24% of the counts from the diffuse component derive from unresolved LMXBs. The diffuse component is asymmetric, with extensions to the NW and SE, as well as a spiral-like structure running SW to NE. These asymmetries are consistent with the diffuse emission arising at least partly from hot gas rather than only unresolved LMXBs.

Three of the resolved sources are coincident with globular clusters found with HST, and an additional six have apparent optical associations on the DSS. The luminosities of the individual sources range from 1.9×10^{38} to 1.8×10^{40} erg s^{-1}, with the central source being the brightest. The luminosity function of the resolved sources is well fit by a broken power-law model with a break radius of approximately twice the Eddington luminosity for spherical accretion of hydrogen dominated gas onto a $1.4 M_\odot$ neutron star. Those sources with luminosities above the break are likely accreting black holes, and those with L_X below the break are probably mainly neutron stars in binary systems. The luminosity function and break luminosity are similar to that seen with *Chandra* in the elliptical NGC 4697 (Sarazin et al. 2000). Thus, the break luminosity make be a general feature of the LMXB populations of early-type galaxies. The break luminosity could be used as a distance indicator, although it is unlikely to be competitive with other techniques, given the large errors associated with the relatively small number of bright LMXBs. In any case, these LMXBs provide a new window on the stellar evolution of early-type galaxies, which is particularly useful for studying the massive stars which were present in these galaxies long ago but which have long since vanished from the optical band.

The composite X-ray spectrum of the resolved sources is best fit with a two component model combining soft blackbody emission with $kT = 0.24$ keV, and a hard, power-law component with a photon index $\Gamma = 1.20$. The luminosity of the sources is dominated by the hard emission. The weakness of the soft emission from the LMXBs suggests that it is unlikely that they dominate the soft emission seen in the X-ray faint galaxies (Fabbiano, Kim, & Trinchieri 1994) as has been suggested by two of us (Irwin & Sarazin 1998a,b).

The strongest source in the field is located at the center of NGC 1553 to within $0\farcs5$. The luminosity (1.75×10^{40} erg s^{-1}) of this source is rather high for an LMXB. The spectrum of this source is very different than that of the LMXBs in the galaxy. It has a hard spectrum with a very high absorbing column. This adds to the evidence that the central source is due to the central AGN in this galaxy, which is a radio source (Harnett 1987) with a LINER-like optical emission spectrum (Phillips et al. 1986).

For the X-ray spectrum of the diffuse emission and of the total (sources plus diffuse) emission, the best fit was achieved with a model combining a soft MEKAL component, with a temperature $kT \approx 0.5$ keV and abundance approximately 10% solar, along with a hard, power-law component. In this case, the soft component is dominant. The total and diffuse spectra show soft X-ray lines complexes which indicate that most of the diffuse emission is due to hot diffuse gas.

Perhaps the most intriguing new result from this observation is the spiral feature in the diffuse emission near the center of the galaxy. We consider several models for the origin of the spiral feature including absorption, thermal evaporation of cooler material, tidal effects, cooling, adiabatic compression, and shocks. Radiative cooling and shear might explain the feature, although the spectral evidence is not consistent with this. It seems most likely that this feature is due to adiabatic or shock compression of ambient gas. We suggest that the spiral is gas which is compressed at the edges of two radio lobes. This is consistent with the radio axis being perpendicular to the dust lane in the nucleus of the galaxy. Unfortunately, there is no high resolution radio image of this southern galaxy; thus, we are in the unusual situation (previous to *Chandra*, at least) of having much higher resolution X-ray than radio data. The radio flux is low enough that energetic arguments suggest that the spiral feature can be explained by an interaction with the radio source only if the present-day source is a fading remnant of previously more intense radio activity.

We are very grateful to Arunav Kundu for providing us with his unpublished list of globular clusters in NGC 1553, for determining the optical position of the nucleus in NGC 1553, and for many very helpful conversations about the HST observations of this galaxy. We thank Maxim Markevitch for several extremely helpful communications concerning the background in the ACIS detector. We are

very grateful to Alexey Vikhlinin for providing his software package for extracting X-ray spectra and constructing the response files for extended sources. We thank Shri Kulkarni for the interesting suggestion that all or most LMXBs are formed in globular clusters. Support for this work was provided by the National Aeronautics and Space Administration through *Chandra* Award Numbers GO0-1019X, GO0-1141X, and GO0-1173X, issued by the *Chandra* X-ray Observatory Center, which is operated by the Smithsonian Astrophysical Observatory for and on behalf of NASA under contract NAS8-39073. J. A. I. was supported by *Chandra* Fellowship grant PF9-10009, awarded through the *Chandra* Science Center.

REFERENCES

Allen, S. W., di Matteo, T., & Fabian, A. C. 2000, MNRAS, 311, 493
Bally, J., & Thronson, Jr., H. A. 1989, AJ, 97, 69
Bettoni, D., & Buson, L. M. 1987, A&AS, 67, 341
Brandt, W. N., et al., 2000, ApJ, 199, 2349
Bridges, T. J., & Hanes, D. A. 1990, AJ, 99, 1100
Canizares, C. R., Fabbiano, G., & Trinchieri, G. 1987, ApJ, 312, 503
Davis, D. S., & White, R. E., III 1996, ApJ, 470, L35
Dickey, J. M., & Lockman, F. J. 1990, ARA&A, 28, 215
Fabbiano, G., Kim, D.-W., & Trinchieri, G. 1994, ApJ, 429, 94
Faber, S. M., Wegner, G., Burstein, D., Davies, R. L., Dressler, A., Lynden-Bell, D., & Terlevich, R. J. 1989, ApJS, 69, 763
Fabian, A. C., Sanders, J. S., Ettori, S., Taylor, G. B., Allen, S. W., Crawford, C. S., Iwasawa, K., Johnstone, R. M., & Ogle, P. M. 2000, MNRAS, 318, L65
Forman, W., Jones, C., & Tucker W. C. 1985, ApJ, 293, 102
Harnett, J. I. 1987, MNRAS, 227, 887
Hasinger, G., Burg, R., Giacconi, R., Schmidt, M., Trümper, J., & Zamorani, G. 1998, A&A, 329, 495
Irwin, J. A., & Sarazin, C. L. 1998a, ApJ, 494, L33
Irwin, J. A., & Sarazin, C. L. 1998b, ApJ, 499, 650
Jorgensen, I., Franx, M., & Kjaergaard, P. 1995, MNRAS, 273, 1097
Kaaret, P., et al., 2000, MNRAS, in press (astro-ph/0009211)
Kim, D.-W. 1989, ApJ, 346, 653
Kim, D.-W., Fabbiano, G., Matsumoto, H., Koyama, K., & Trinchieri, G. 1996, ApJ, 468, 175
Kim, D.-W., Fabbiano, G., & Trinchieri, G. 1992, ApJ, 393, 134
Kormendy, J. 1984, ApJ, 286, 116
Kulkarni, S. 2000, private communication
Longo, G., Zaggia, S. R., Busarello, G., & Richter, G. 1994, A&AS, 105, 433
Macchetto, F., Pastoriza, M., Caon, N., Sparks, W. B., Giavalisco, M., Bender, R., & Capaccioli, M. 1996, A&AS, 120, 463
Malin, D. F., & Carter, D. 1983, ApJ, 274, 534
Markevitch, M. 2000, ACIS Background, http://asc.harvard.edu/cal/Links/Acis/acis/Cal_prods/bkgrnd/04_11/ bg110400.html
Markevitch, M., Sarazin, C. L., & Vikhlinin, A. 1999, ApJ, 521, 526
Markevitch, M., et al., 2000, ApJ, 541, 542
Matsumoto, H., Koyama, K., Awaki, H., & Tsuru, T., Loewenstein, M., & Matsushita, K. 1997, ApJ, 482, 133
McNamara, B. R., Wise, M., Nulsen, P. E. J., David, L. P., Sarazin, C. L., Bautz, M., Markevitch, M., Forman, W. R. Jones, C., & Harris D. E. 2000, ApJ, 534, L135
Mushotzky, R. F., Cowie, L. L., Barger, A. J., & Arnaud, K. A. 2000, Nature, 404, 459
Pellegrini, S. 1994, A&A, 292, 395
Phillips, M. M., Jenkins, C. R., Dopita, M. A., Sadler, E. M., & Binette, L. 1986, AJ, 91, 1062
Quillen, A. C., Bower, G. A., & Stritzinger, M. 2000, ApJS, 128, 85
Roberts, M. S., Hogg, D. E., Bregman, J. N., Forman, W. R., & Jones, C. 1991, ApJS, 75, 751
Sarazin, C. L. 1990, in The Interstellar Medium in Galaxies, ed. H. A. Thronson, Jr., & J. M. Shull (Dordrecht: Kluwer), 201
Sarazin, C. L., Irwin, J. A., & Bregman, J. N. 2000, ApJ, 544, L101
Sparks, W. B. 1997, in Galactic and Cluster Cooling Flows, ed. N. Soker (San Francisco: ASP Conf. Ser. Vol. 115), 192
Sparks, W. B., Macchetto, F., & Golombek, D. 1989, ApJ, 345, 153
Tonry, J. L., Dressler, A., Blakeslee, J. P., Ajhar, E. A., Fletcher, A. B., Luppino, G. A., Metzger, M. R., Moore, C. B. 2001, ApJ, in press (astro-ph/0011223)
Trinchieri, G., & Fabbiano, G. 1985, ApJ, 296, 447
Trinchieri, G., Noris, L., & di Serego Alighieri, S. 1997, A&A, 326, 565
Trinchieri, G., Pellegrini, S., Wolter, A., Fabbiano, G., & Fiore, F. 2000, A&A, in press (astro-ph/0010234)
Vikhlinin, A., Markevitch, M., & Murray, S. S. 2000, ApJ, submitted (astro-ph/0008496)
White, R. E., III, Kulkarni, S. R., & Sarazin, C. L. 2001, in preparation
Wise, M. W., Davis, J. E., Huenemoerder, D. P., Houck, J. C., & Dewey, D. 2000, MARX 3.0 Technical Manual, http://space.mit.edu/ASC/MARX

TABLE 1
NGC 1553: DISCRETE X-RAY SOURCES

Src. No. (1)	Src. Name (2)	RA(J2000) (h:m:s) (3)	Dec(J2000) (°:′:″) (4)	d (″) (5)	Count Rate (10^{-4} s^{-1}) (6)	SNR (7)	L_X (0.3-10 keV) (10^{38} erg s^{-1}) (8)	Notes (9)
1	CXOU J041610.5-554646	4:16:10.59	-55:46:46.8	0.0	356.41±12.50	28.5	175.07	
2	CXOU J041609.9-554646	4:16:09.98	-55:46:46.6	5.2	17.95±2.90	6.2	8.82	
3	CXOU J041610.4-554639	4:16:10.43	-55:46:39.0	7.9	15.07±2.67	5.6	7.40	
4	CXOU J041609.6-554642	4:16:09.69	-55:46:42.2	8.9	7.64±1.94	3.9	3.75	HST,var
5	CXOU J041610.1-554637	4:16:10.14	-55:46:37.5	10.1	9.04±2.08	4.3	4.44	
6	CXOU J041611.7-554652	4:16:11.76	-55:46:52.5	11.4	10.02±2.21	4.5	4.92	
7	CXOU J041612.0-554658	4:16:12.05	-55:46:58.5	16.9	5.47±1.62	3.4	2.69	
8	CXOU J041612.8-554647	4:16:12.86	-55:46:47.4	19.2	8.46±2.03	4.2	4.15	
9	CXOU J041607.7-554643	4:16:07.75	-55:46:43.0	24.2	4.79±1.56	3.1	2.35	
10	CXOU J041610.9-554621	4:16:10.92	-55:46:21.6	25.3	4.42±1.50	2.9	2.17	
11	CXOU J041611.0-554712	4:16:11.08	-55:47:12.0	25.5	4.56±1.50	3.0	2.24	HST
12	CXOU J041609.5-554621	4:16:09.52	-55:46:21.1	27.3	5.43±1.62	3.3	2.67	
13	CXOU J041606.1-554626	4:16:06.18	-55:46:26.1	42.6	3.97±1.37	2.9	1.95	
14	CXOU J041608.3-554604	4:16:08.31	-55:46:04.9	46.2	4.28±1.44	3.0	2.10	
15	CXOU J041607.1-554610	4:16:07.15	-55:46:10.1	46.8	11.03±2.26	4.9	5.42	
16	CXOU J041616.3-554618	4:16:16.38	-55:46:18.4	56.5	40.04±4.22	9.5	19.67	
17	CXOU J041602.9-554655	4:16:02.90	-55:46:55.1	65.4	66.51±5.41	12.3	32.67	var
18	CXOU J041611.7-554753	4:16:11.77	-55:47:53.5	67.5	7.24±1.83	4.0	3.56	
19	CXOU J041615.6-554741	4:16:15.65	-55:47:41.5	69.4	4.46±1.52	2.9	2.19	
20	CXOU J041612.2-554516	4:16:12.25	-55:45:16.7	91.1	4.94±1.52	3.2	2.43	
21	CXOU J041608.3-554816	4:16:08.31	-55:48:16.8	92.0	29.11±3.58	8.1	14.30	
22	CXOU J041559.2-554615	4:15:59.26	-55:46:15.2	100.7	10.74±2.24	4.8	5.27	DSS
23	CXOU J041621.5-554731	4:16:21.52	-55:47:31.9	102.7	6.14±1.68	3.7	3.02	HST
24	CXOU J041611.5-554832	4:16:11.51	-55:48:32.9	106.4	9.79±2.12	4.6	4.81	
25	CXOU J041623.2-554725	4:16:23.21	-55:47:25.3	113.2	6.56±1.74	3.8	3.22	
26	CXOU J041620.9-554805	4:16:20.99	-55:48:05.3	117.7	12.56±2.37	5.3	6.17	
27	CXOU J041604.1-554458	4:16:04.17	-55:44:58.6	121.0	9.46±2.22	4.3	4.65	DSS
28	CXOU J041602.0-554508	4:16:02.00	-55:45:08.1	122.5	5.85±1.72	3.4	2.88	
29	CXOU J041616.5-554839	4:16:16.51	-55:48:39.3	123.0	17.25±2.77	6.2	8.47	
30	CXOU J041615.6-554425	4:16:15.67	-55:44:25.4	147.8	11.92±2.40	5.0	5.86	
31	CXOU J041630.5-554613	4:16:30.52	-55:46:13.6	171.4	20.32±3.03	6.7	9.98	
32	CXOU J041631.3-554703	4:16:31.31	-55:47:03.8	175.6	8.89±2.02	4.4	4.37	
33	CXOU J041602.6-554932	4:16:02.65	-55:49:32.4	178.6	11.34±2.26	5.0	5.57	
34	CXOU J041615.9-554949	4:16:15.94	-55:49:49.6	188.3	7.86±1.89	4.2	3.86	DSS
35	CXOU J041602.8-554947	4:16:02.83	-55:49:47.8	192.4	23.96±3.40	7.0	11.77	DSS
36	CXOU J041617.9-554955	4:16:17.91	-55:49:55.1	198.2	7.97±1.90	4.2	3.91	var
37	CXOU J041626.0-554406	4:16:26.05	-55:44:06.5	206.7	5.38±1.69	3.2	2.64	
38	CXOU J041551.5-554859	4:15:51.53	-55:48:59.7	208.5	193.17±9.71	19.9	94.89	DSS
39	CXOU J041547.3-554810	4:15:47.38	-55:48:10.3	212.8	5.94±1.72	3.5	2.92	
40	CXOU J041545.5-554543	4:15:45.56	-55:45:43.9	220.4	12.48±2.55	4.9	6.13	var
41	CXOU J041611.5-555029	4:16:11.50	-55:50:29.4	222.8	12.16±2.36	5.2	5.97	var
42	CXOU J041635.5-554440	4:16:35.56	-55:44:40.5	245.7	8.55±2.08	4.1	4.20	
43	CXOU J041637.9-554520	4:16:37.90	-55:45:20.7	246.0	6.64±1.87	3.6	3.26	
44	CXOU J041640.4-554510	4:16:40.41	-55:45:10.5	269.5	8.30±2.04	4.1	4.08	
45	CXOU J041538.2-554539	4:15:38.25	-55:45:39.1	281.1	5.98±2.05	2.9	2.94	DSS
46	CXOU J041540.3-554847	4:15:40.37	-55:48:47.0	281.7	7.84±2.27	3.5	3.85	
47	CXOU J041643.2-554510	4:16:43.21	-55:45:10.5	291.6	9.84±2.25	4.4	4.83	
48	CXOU J041603.3-554110	4:16:03.31	-55:41:10.7	341.7	43.52±4.90	8.9	21.38	DSS
49	CXOU J041557.2-554123	4:15:57.21	-55:41:23.4	342.5	8.18±2.32	3.5	4.02	

NOTE.—In column (9), "HST" indicates that the source is identified with a globular cluster from HST data, "DSS" indicates that there is an apparent optical identification on the DSS image, and "var" means that the source may be variable.

TABLE 2
SPECTRAL FITS

Component	N_H (10^{20} cm^{-2})	Soft Model	kT_s (keV)	Abund. (solar)	Γ	χ^2/d.o.f.	Total Cts. (0.7-10.0 keV)
total	(1.41)	mekal	$0.48^{+0.05}_{-0.10}$	$0.05^{+0.06}_{-0.03}$	$0.63^{+0.33}_{-0.19}$	315.6/260	3616
total	(1.41)	mekal	$0.47^{+0.04}_{-0.13}$	$0.16^{+0.33}_{-0.05}$	(1.20)	321.9/261	3616
diffuse	(1.41)	mekal	$0.48^{+0.04}_{-0.09}$	$0.06^{+0.06}_{-0.04}$	$-0.35^{+0.86}_{-1.32}$	263.4/229	2328
diffuse	(1.41)	mekal	$0.47^{+0.04}_{-0.10}$	$0.10^{+0.06}_{-0.05}$	(1.20)	270.8/230	2328
sources	(1.41)	bbody	$0.24^{+0.05}_{-0.07}$		$1.20^{+0.39}_{-0.15}$	35.2/40	1332
AGN	$18.25^{+7.42}_{-7.59}$	diskbb	$1.70^{+0.39}_{-0.22}$			34.7/32	758
AGN	$36.04^{+12.95}_{-9.22}$				$1.59^{+0.11}_{-0.18}$	40.3/32	758
spiral	(1.41)	mekal	$0.51^{+0.07}_{-0.09}$	$0.12^{+0.17}_{-0.07}$	$-1.55^{+1.57}_{-0.25}$	19.5/24	465
spiral	(1.41)	mekal	$0.50^{+0.06}_{-0.06}$	$0.38^{+0.28}_{-0.14}$	(1.20)	27.1/25	465
central circle	(1.41)	mekal	$0.48^{+0.07}_{-0.09}$	$0.10^{+0.34}_{-0.07}$	$1.38^{+1.54}_{-2.12}$	38.6/43	572
central circle	(1.41)	mekal	$0.49^{+0.07}_{-0.08}$	$0.10^{+0.06}_{-0.04}$	(1.20)	38.7/44	572

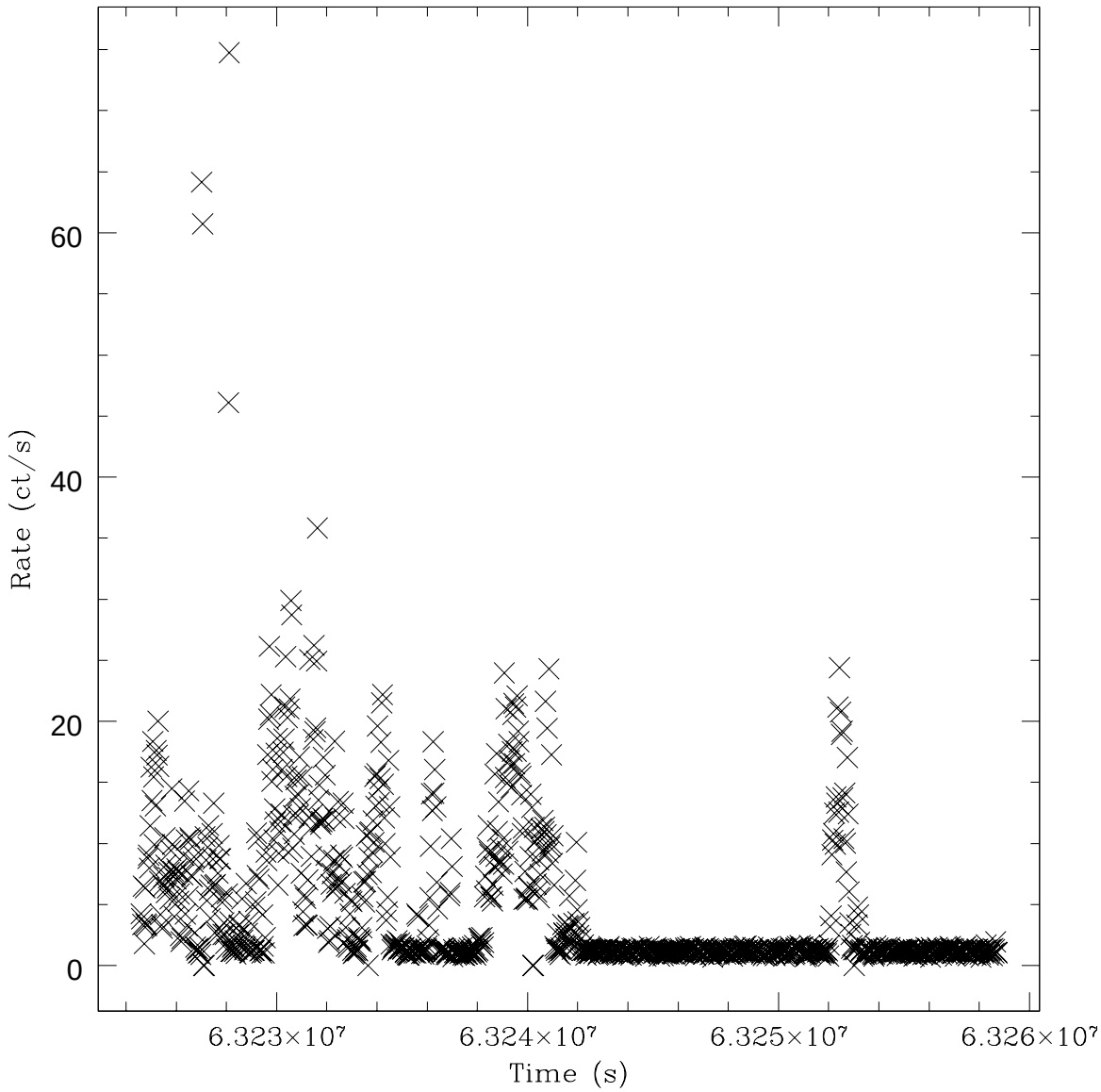

FIG. 1.— Light curve of the total X-ray emission detected by the ACIS S3 chip in the 0.3-10.0 keV band. The time is measured in seconds. Background flares are evident, particularly during the first half of the exposure. The quiescent rate is about 1.19 ct s^{-1}.

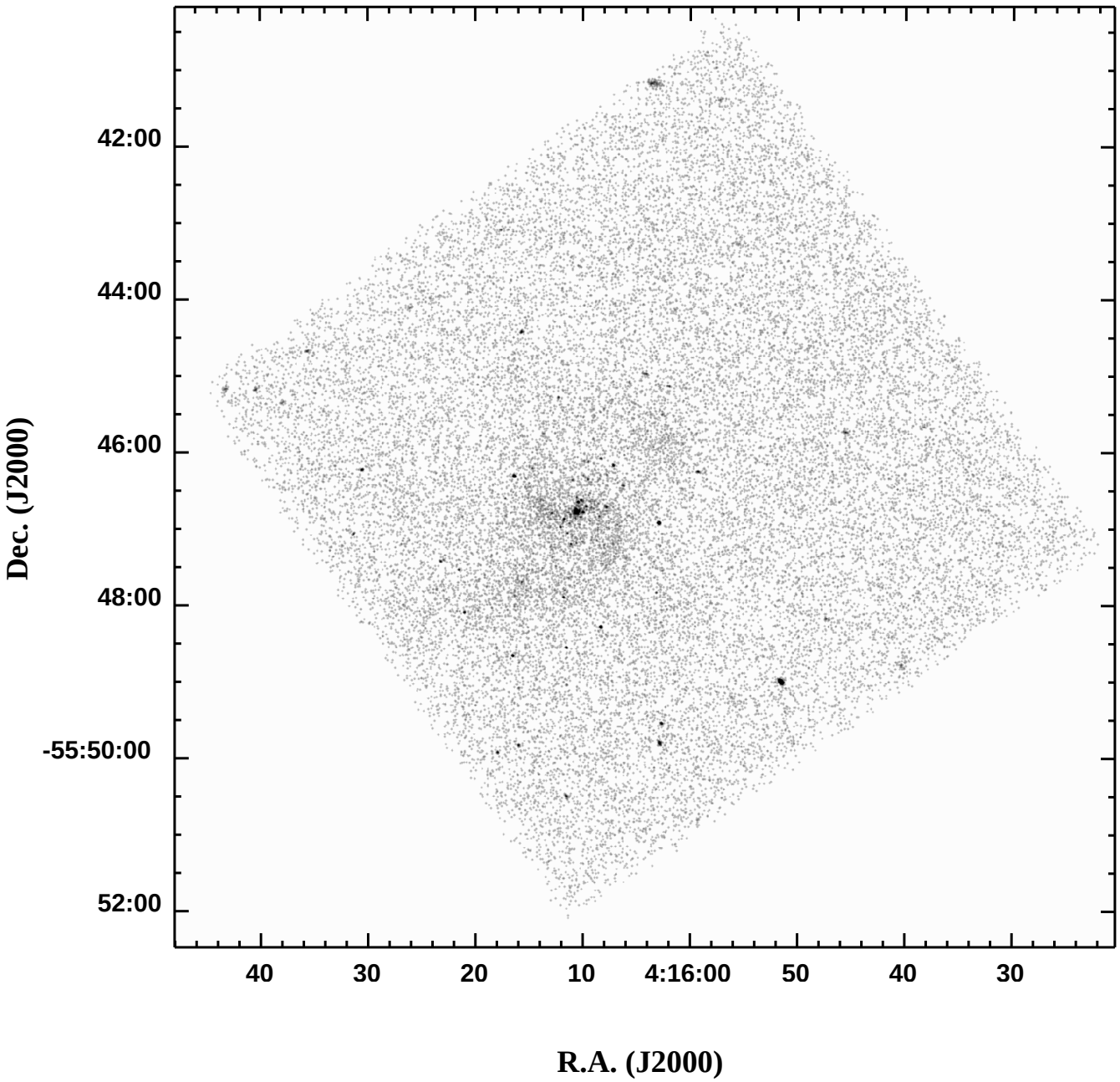

FIG. 2.— Slightly smoothed ($\sigma = 0\farcs492 = 1$ pixel Gaussian) *Chandra* S3 image of NGC 1553. Discrete sources as well as asymmetric diffuse emission are apparent. The center of the galaxy is located to the SE of the detector center, and is coincident with the brightest point source in the field.

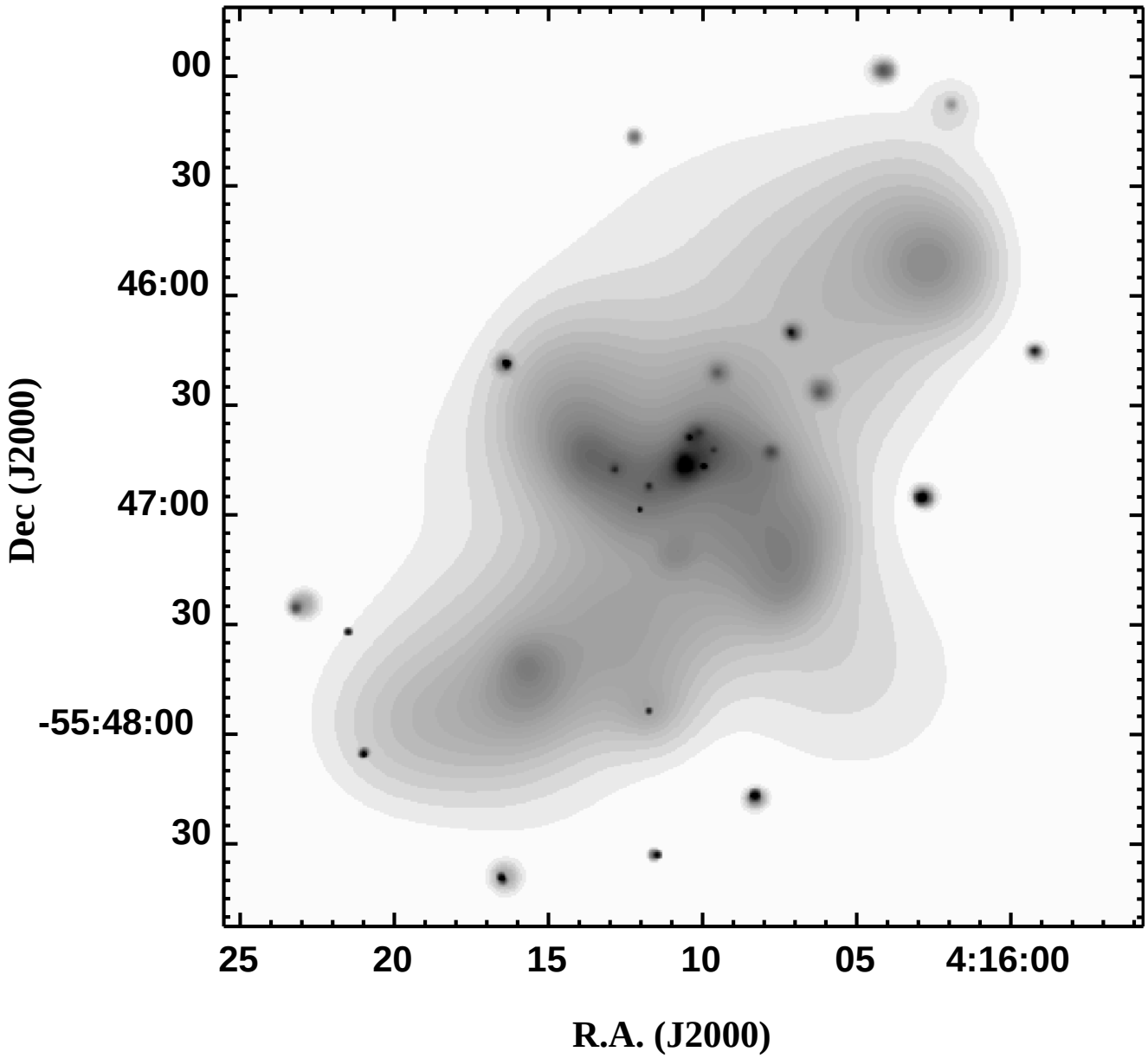

FIG. 3.— Adaptively smoothed image of the $4' \times 4'$ region surrounding the center of NGC 1553. The image has been corrected for exposure and background. The grayscale is logarithmic and ranges from 3.8×10^{-7} to 3.0×10^{-3} ct pix^{-1} s^{-1}.

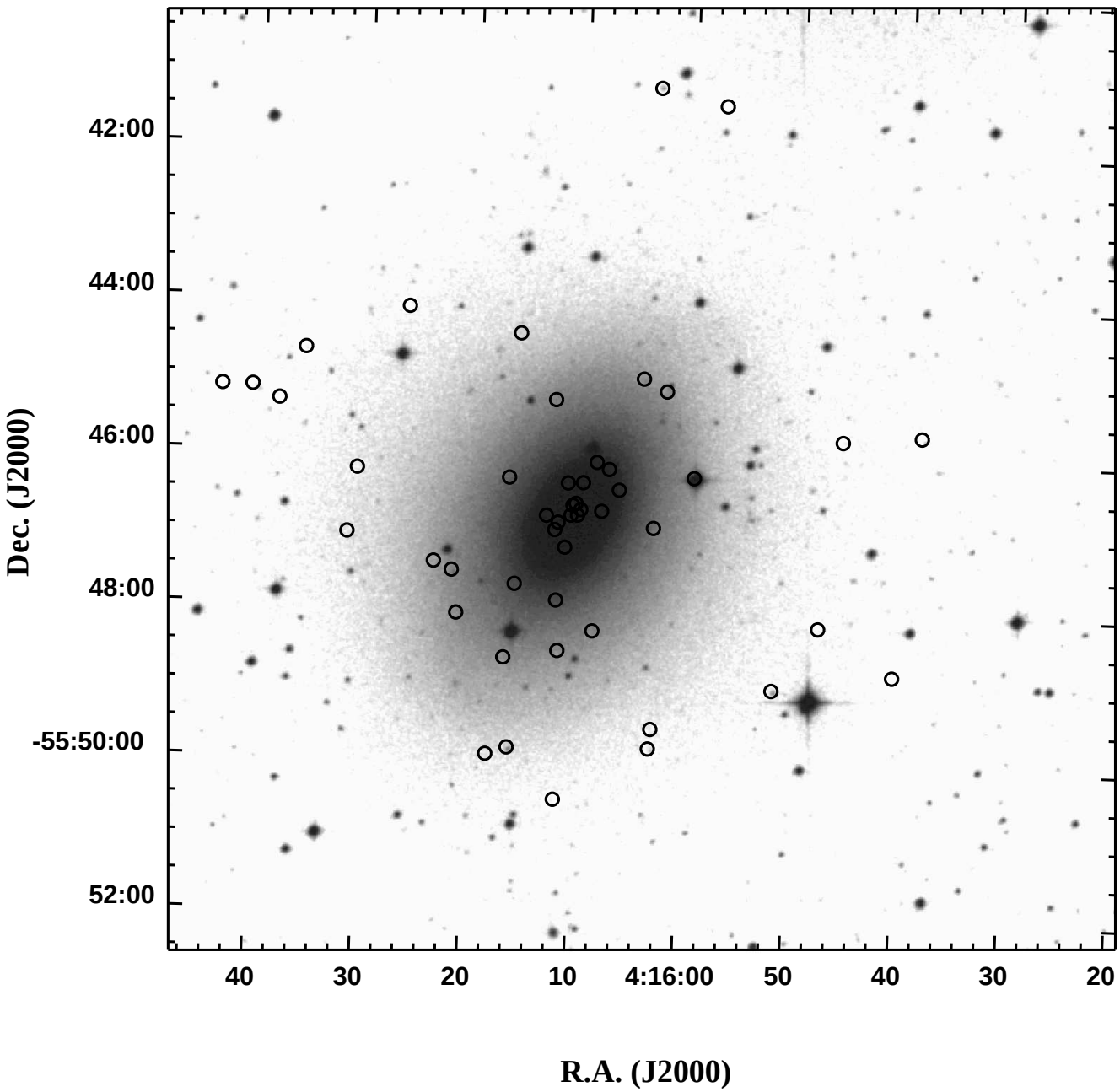

FIG. 4.— The positions of the X-ray sources are overlaid as circles onto the DSS optical image of NGC 1553.

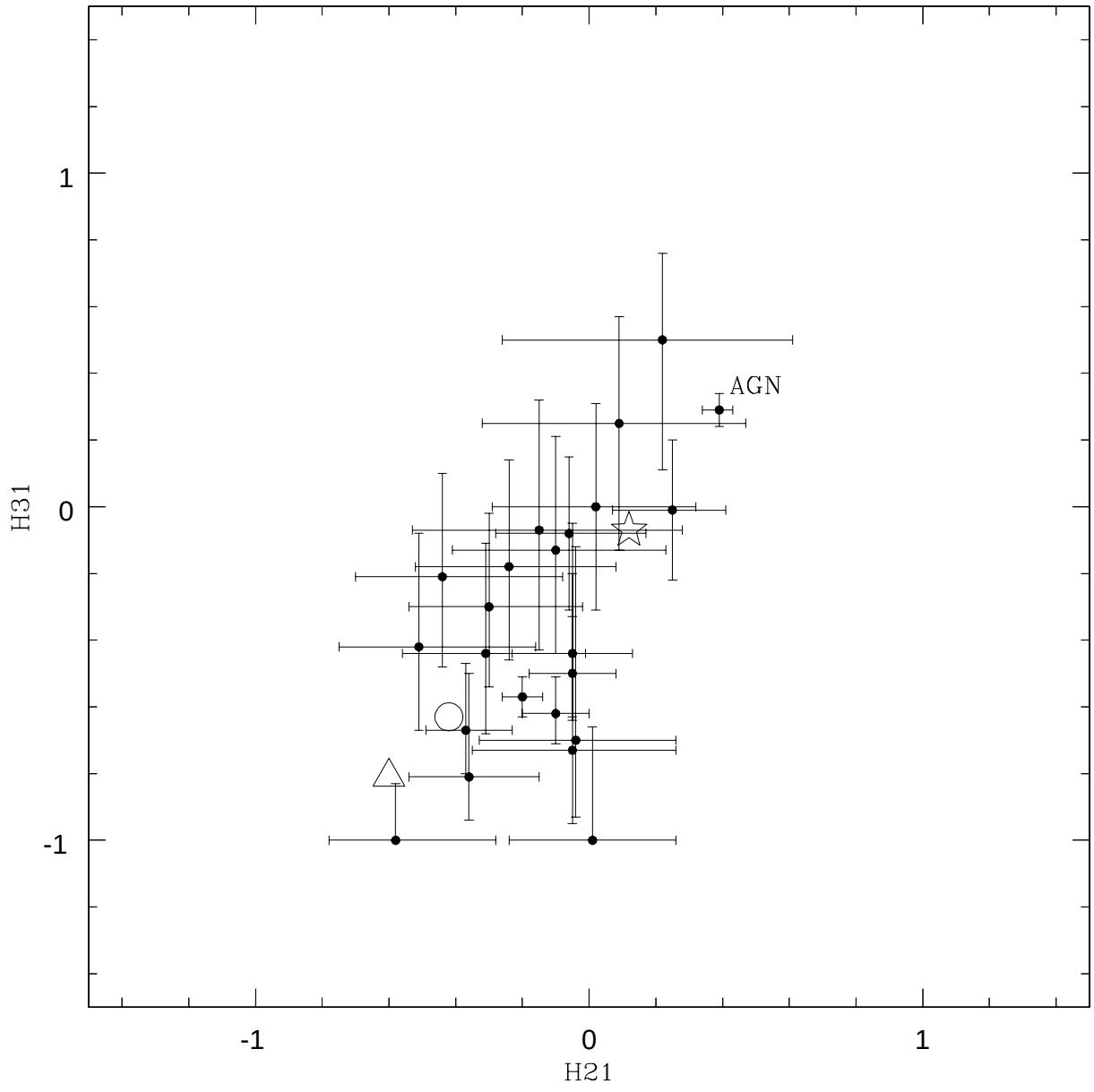

FIG. 5.— X-ray hardness ratios of the discrete sources detected with more than 20 counts in the S3 CCD in the 0.3 - 10.0 keV band. The hardness ratios are $H21 = (M - S)/(M + S)$, and $H31 = (H - S)/(H + S)$. The point marked "AGN" is the central source in NGC 1553. For comparison, the open circle shows the hardness ratios for the total emission, the open triangle shows those for the diffuse emission, and the open star shows the ratios for the sum of the discrete sources.

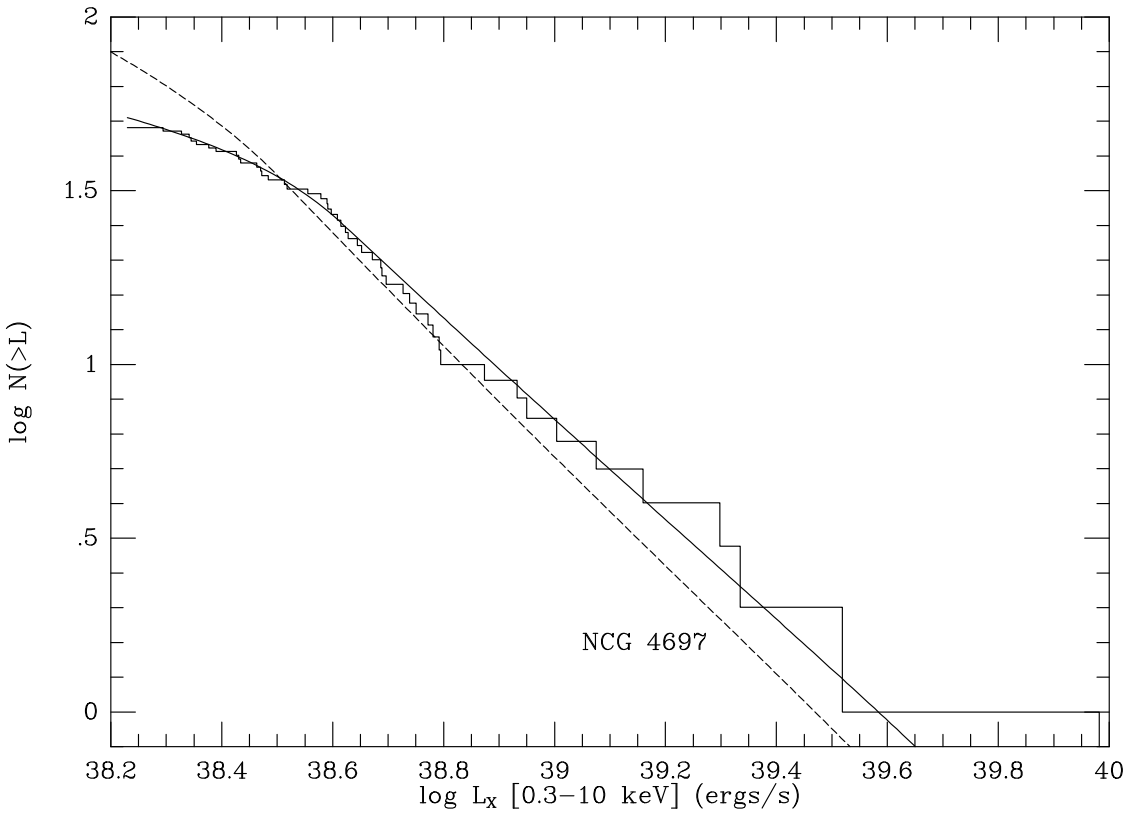

FIG. 6.— The histogram is the luminosity function of the discrete X-ray sources in NGC1553. The solid curve represents the best-fitting broken power-law function. For comparison, the dashed line shows the broken power-law fit for NGC 4697 (Sarazin et al. 2000).

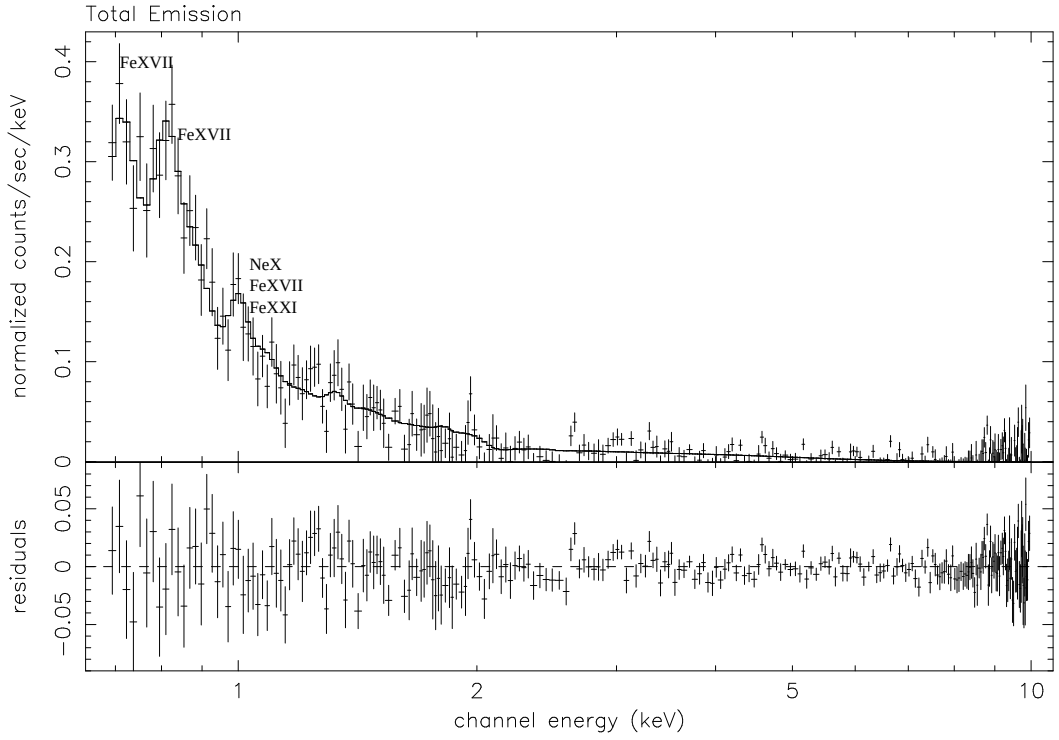

FIG. 7.— X-ray spectrum of the total emission (diffuse plus resolved sources) from within two effective radii. The points with error bars in the upper panel are the data, while the solid histogram is the best fit model including Galactic absorption, a MEKAL soft emission component, and a power-law hard component. The lower panel shows the residuals to the model.

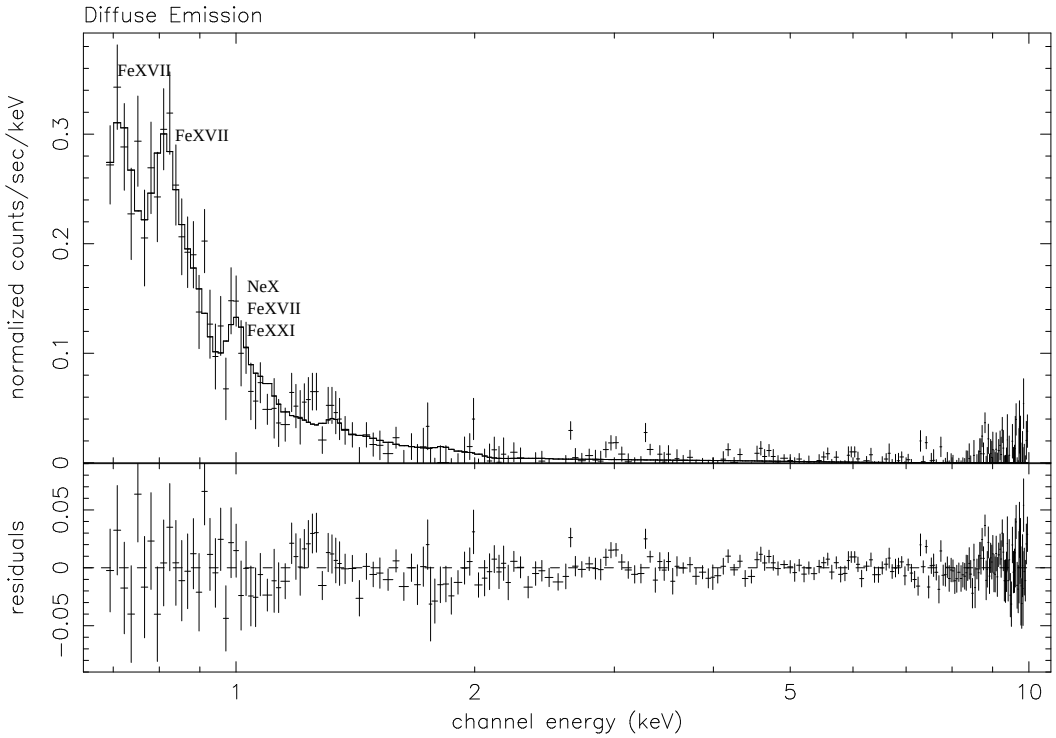

FIG. 8.— Spectrum of the diffuse emission within two effective radii fit with a model combining Galactic absorption, a MEKAL soft component, and a hard power-law hard component.

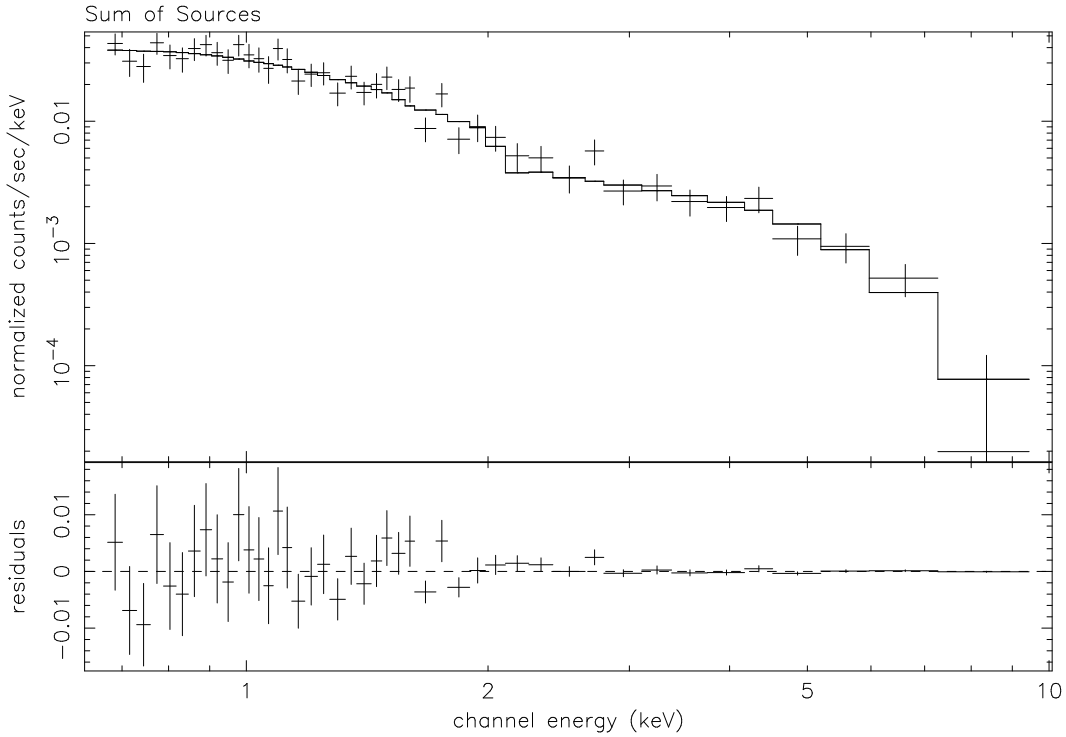

FIG. 9.— Spectrum extracted from a sum of the sources, excluding the central source and the bright Src. 38 fit with a model combining Galactic absorption, soft blackbody emission, and a hard power-law.

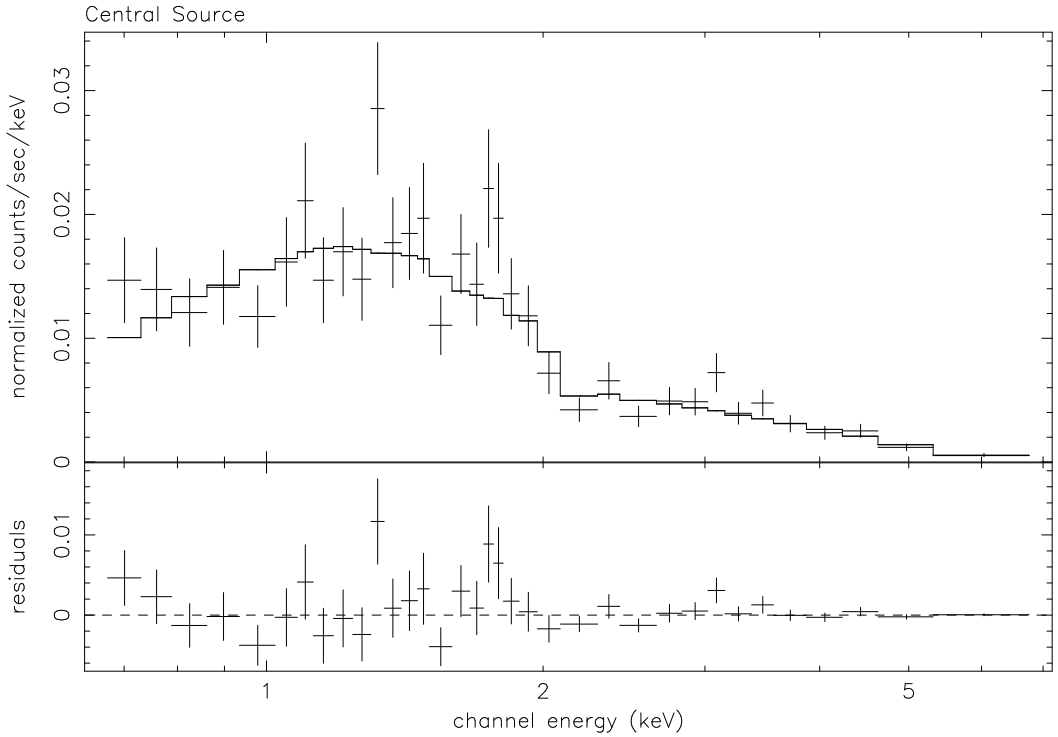

FIG. 10.— Spectrum of the bright, central resolved source fit with a model combining a high absorbing column and disk blackbody emission.